

# IL-23 stabilizes an effector T<sub>reg</sub> cell program in the tumor microenvironment

Received: 20 January 2023

Accepted: 12 January 2024

Published online: 14 February 2024

 Check for updates

Tobias Wertheimer<sup>1,8</sup>, Pascale Zwicky<sup>1,8</sup>, Lukas Rindlisbacher<sup>1</sup>, Colin Sparano<sup>1</sup>, Marijine Vermeer<sup>1</sup>, Bruno Marcel Silva de Melo<sup>1,2</sup>, Claudia Haftmann<sup>1</sup>, Tamina Rückert<sup>3</sup>, Aakriti Sethi<sup>1</sup>, Stefanie Schärli<sup>1</sup>, Anna Huber<sup>1</sup>, Florian Ingelfinger<sup>1</sup>, Caroline Xu<sup>1</sup>, Daehong Kim<sup>1</sup>, Philipp Häne<sup>1</sup>, André Fonseca da Silva<sup>1</sup>, Andreas Muschaweckh<sup>4</sup>, Nicolas Nunez<sup>1</sup>, Sinduya Krishnarajah<sup>1</sup>, Natalie Köhler<sup>3,5</sup>, Robert Zeiser<sup>3,5</sup>, Mohamed Oukka<sup>6</sup>, Thomas Korn<sup>4,7</sup>, Sonia Tugues<sup>1,9</sup>✉ & Burkhard Becher<sup>1,9</sup>✉

Interleukin-23 (IL-23) is a proinflammatory cytokine mainly produced by myeloid cells that promotes tumor growth in various preclinical cancer models and correlates with adverse outcomes. However, as to how IL-23 fuels tumor growth is unclear. Here, we found tumor-associated macrophages to be the main source of IL-23 in mouse and human tumor microenvironments. Among IL-23-sensing cells, we identified a subset of tumor-infiltrating regulatory T (T<sub>reg</sub>) cells that display a highly suppressive phenotype across mouse and human tumors. The use of three preclinical models of solid cancer in combination with genetic ablation of *IL23r* in T<sub>reg</sub> cells revealed that they are responsible for the tumor-promoting effect of IL-23. Mechanistically, we found that IL-23 sensing represents a crucial signal driving the maintenance and stabilization of effector T<sub>reg</sub> cells involving the transcription factor Foxp3. Our data support that targeting the IL-23/IL-23R axis in cancer may represent a means of eliciting antitumor immunity.

Regulatory T (T<sub>reg</sub>) cells are a functionally distinct T cell population expressing the transcription factor Foxp3 that are critically involved in maintaining immune homeostasis<sup>1</sup>. Like conventional T cells, T<sub>reg</sub> cells can undergo functional activation after T cell antigen receptor (TCR) stimulation, converting naive to highly suppressive effector T<sub>reg</sub> (eT<sub>reg</sub>) cells<sup>2</sup>. This cellular subset is marked by augmented expression of Foxp3, CTLA-4, interleukin-10 (IL-10), ICOS and TIGIT (among others) and represents the dominant T<sub>reg</sub> cell subpopulation in non-lymphoid tissues and tumors<sup>3,4</sup>.

In the context of cancer, both mouse and human tumor microenvironments (TMEs) are enriched with T<sub>reg</sub> cells, contributing to an immunosuppressive niche suppressing antitumor immune responses and limiting therapeutic success of immunotherapy<sup>5,6</sup>. Although generalized T<sub>reg</sub> cell depletion has proven to be efficacious in most preclinical tumor models<sup>7–9</sup>, it also induces systemic inflammation<sup>10</sup>. Consequently, strategies to reduce their suppressive capacities or destabilize T<sub>reg</sub> cells specifically in the TME are attractive targets for cancer immunotherapy.

<sup>1</sup>Department of Inflammation Research, Institute of Experimental Immunology, University of Zurich, Zurich, Switzerland. <sup>2</sup>Department of Pharmacology, Center for Research in Inflammatory Diseases, Ribeirao Preto Medical School, University of Sao Paulo, Sao Paulo, Brazil. <sup>3</sup>Department of Internal Medicine I, Hematology, Oncology, and Stem Cell Transplantation, Faculty of Medicine, Medical Centre, University of Freiburg, Freiburg, Germany. <sup>4</sup>Institute for Experimental Neuroimmunology, Klinikum Rechts der Isar, Technical University of Munich, Munich, Germany. <sup>5</sup>Centre for Integrative Biological Signalling Studies (CIBSS), University of Freiburg, Freiburg, Germany. <sup>6</sup>Department of Immunology, University of Washington, Seattle, WA, USA. <sup>7</sup>Munich Cluster for Systems Neurology (SyNergy), Munich, Germany. <sup>8</sup>These authors contributed equally: Tobias Wertheimer, Pascale Zwicky. <sup>9</sup>These authors jointly supervised this work: Sonia Tugues, Burkhard Becher. ✉e-mail: [tugues@immunology.uzh.ch](mailto:tugues@immunology.uzh.ch); [becher@immunology.uzh.ch](mailto:becher@immunology.uzh.ch)

IL-23 is a member of the IL-12 superfamily of cytokines, which is primarily produced by cells of the mononuclear phagocyte system<sup>11</sup>. IL-23 drives the pathophysiology of immune disorders, such as psoriasis and inflammatory bowel disease, by inducing a pathogenic lymphocyte program promoting tissue inflammation<sup>12,13</sup>. Paradoxically, in the context of cancer, IL-23 exerts tumor-promoting functions. As such, ablation of both IL-23 or its receptor leads to reduced tumor burden<sup>14–17</sup>. The tumor-promoting effects of IL-23 appear to be independent of IL-17 (ref. 16), and ablation of IL-23 is associated with an enhanced infiltration of CD8<sup>+</sup> T cells, natural killer (NK) cells and T<sub>reg</sub> cells<sup>14,15,17</sup>.

To understand the mechanisms underpinning the protumorigenic functions of IL-23, we systematically interrogated both the cellular sources and sensors of IL-23 in mouse and human TMEs. We identified tumor-associated macrophages (TAMs) as the main cellular source of IL-23 and tumor-infiltrating T<sub>reg</sub> cells as an IL-23 receptor (IL-23R)-expressing cell type. IL-23 stabilizes eT<sub>reg</sub> cell identity and Foxp3 expression, thus enhancing immunosuppression, resulting in decreased antitumor immunity. Our findings render the IL-23/IL-23R axis a promising therapeutic target for the selective destabilization of tumor-infiltrating eT<sub>reg</sub> cells for cancer immunotherapy.

## Results

### IL-23R marks a highly activated T<sub>reg</sub> subset in the mouse TME

To identify the cellular sources of IL-23 in the TME, we investigated the expression of *Il23a* (encoding IL-23p19) in single-cell RNA-sequencing (scRNA-seq) data of tumor-infiltrating myeloid cells in the mouse B16-F10 tumor model<sup>18</sup> (hereafter B16; Fig. 1a–c) and mouse pan-tumor T cells from 21 cancer entities<sup>19</sup> (Extended Data Fig. 1c). We identified two TAM, four monocyte and three dendritic cell (DC) clusters (Fig. 1a and Extended Data Fig. 1a,b). Although the expression of *Il23a* was generally low, we assigned two TAM populations (Spp1<sup>+</sup> and Clq<sup>+</sup> TAMs) as the major *Il23a*-producing cells in the TME (Fig. 1b,c). In addition, monocytes (*Hp*<sup>+</sup> and *Ccl7*<sup>+</sup> monocytes) and conventional type 2 DCs (cDC2s) contributed to the total *Il23a* expression in the TME (Fig. 1b,c), with only negligible amounts in tumor-infiltrating T cells (TILs; Extended Data Fig. 1c).

In line with previous findings<sup>20</sup>, we found that flow cytometry using anti-IL-23R, previously used by others<sup>21–23</sup>, failed to faithfully detect IL-23R as no IL-23R expression was observed in skin γδ<sup>intermediate</sup> (Vγ4/Vγ6) T cells (Extended Data Fig. 1d)<sup>24</sup>. Therefore, we generated an IL-23R reporter mouse strain where endogenous mouse *Il23r* was replaced by a gene construct composed of human *IL23R* cDNA and tdTomato (hereafter IL-23R<sup>tdTomato</sup> mice; Extended Data Fig. 1e). In line with previous studies<sup>24</sup>, we detected IL-23R<sup>tdTomato</sup> signal in γδ<sup>intermediate</sup> T cells but not γδ<sup>high</sup> (Vγ5 T cells/dendritic epidermal T cells) or αβ T cells of steady-state mouse skin (Extended Data Fig. 1f). To reliably capture all T cell subsets including T<sub>reg</sub> cells within the TME, we crossed IL-23R<sup>tdTomato</sup> mice with *Foxp3*<sup>DTR-GFP</sup> mice and analyzed TILs (CD45<sup>+</sup>TCRβ<sup>+</sup>TCRγδ<sup>+</sup> cells) after challenge with B16 melanoma (Fig. 1d–f and Extended Data Fig. 1g). Uniform manifold approximation and projection (UMAP) dimensionality reduction followed by FlowSOM metaclustering<sup>25,26</sup> revealed that, besides γδ T cells and CD4<sup>+</sup> effector memory T (T<sub>EM</sub>) cells,

tumor-infiltrating Foxp3<sup>+</sup> T<sub>reg</sub> cells also expressed IL-23R, representing a sizable fraction of total IL-23R-expressing T cells in the TME (Fig. 1e,f). Only minimal *Il23r* expression was detected in myeloid cells (Extended Data Fig. 1h). We also found *Il23r* to be expressed in purified T<sub>reg</sub> cells from tumors of B16 tumor-bearing *Foxp3*<sup>DTR-GFP</sup> mice, whereas those from steady-state lymph nodes (LNs) and tumor-draining LNs (tdLNs) were low in *Il23r* expression (Extended Data Fig. 1i,j).

We next compared the expression of several key mediators of T<sub>reg</sub> activation and suppressive functions between IL-23R<sup>+</sup> and IL-23R<sup>-</sup> T<sub>reg</sub> cells (Fig. 1g and Extended Data Fig. 1k). IL-23R<sup>+</sup> T<sub>reg</sub> cells exhibited a strongly activated phenotype marked by the expression of GITR, ICOS, PD-1, CD39, CD73, CCR8, CD44 and CD69, among others (Fig. 1g). Further analysis of bulk RNA-seq data from sorted T<sub>reg</sub> cells of B16 tumors or spleens<sup>27</sup> confirmed high expression of *Il23r* in tumor-infiltrating T<sub>reg</sub> cells, which was accompanied by an induction of key eT<sub>reg</sub> genes, such as *Pdcd1* (encoding PD-1), *Tnfrsf9* (encoding 4-1BB), *Jcos* and *Lag3* (Fig. 1h). Using immunofluorescence analysis of Foxp3, CD3 and IL-23R<sup>tdTomato</sup> in tdLNs or B16 tumors from IL-23R<sup>tdTomato</sup> reporter mice, we found IL-23R<sup>tdTomato</sup>-expressing T<sub>reg</sub> cells in both tdLNs (Extended Data Fig. 1l) and tumors (Fig. 1i). Taken together, we identified TAMs as the major producers of IL-23 and found that IL-23R designates a highly activated T<sub>reg</sub> cell subset in the mouse TME.

### T<sub>reg</sub> cells mediate the tumor-promoting functions of IL-23

We next sought to elucidate the contribution of IL-23R signaling in T<sub>reg</sub> cells to tumor progression by generating mice in which *Il23r* was specifically deleted in T<sub>reg</sub> cells (*Foxp3*<sup>Cre-YFP</sup>*Il23r*<sup>fl/fl</sup>). The specificity of the conditional gene targeting was shown on T<sub>reg</sub> cells, γδ T cells and CD4<sup>+</sup> and CD8<sup>+</sup> T cells sorted by fluorescence-activated cell sorting (FACS; Extended Data Fig. 2a,b). To model different cancer environments, we used the poorly immunogenic B16 melanoma model and the two highly infiltrated YUMMER1.7 and MC38 tumor models (Fig. 2a). We found that tumor volume and weight were drastically reduced in *Il23r*<sup>del/del</sup> mice compared to in *Il23r*<sup>fl/fl</sup> mice in all three tumor models (Fig. 2b–d), thus confirming the previously reported protumorigenic function of IL-23/IL-23R signaling<sup>14–17</sup>. Importantly, T<sub>reg</sub>-specific ablation of *Il23r* led to an equally reduced tumor burden, phenocopying the kinetics observed in *Il23r*<sup>del/del</sup> mice, suggesting that T<sub>reg</sub> cells are the relevant target of IL-23 (Fig. 2b–d and Extended Data Fig. 2c). Blockade of IL-23 with anti-p19 leads to a similar reduction in tumor growth (Extended Data Fig. 2e). To exclude the potential influence of Cre-mediated toxicity, we confirmed reduced tumor growth in the absence of *Il23r* in T<sub>reg</sub> cells in *Foxp3*<sup>Cre-YFP</sup> and *Foxp3*<sup>Cre-YFP</sup>*Il23r*<sup>fl/fl</sup> mice (Extended Data Fig. 2d).

In summary, we found that T<sub>reg</sub> cells mediate the tumor-promoting functions of IL-23 across different preclinical cancer models.

### IL-23R signaling in T<sub>reg</sub> cells suppresses antitumor immunity

To investigate the mechanism by which IL-23R signaling in T<sub>reg</sub> cells alters antitumor immunity, we profiled TILs of *Foxp3*<sup>Cre-YFP</sup>*Il23r*<sup>fl/fl</sup> mice and *Il23r*<sup>fl/fl</sup> controls. We identified eight T cell clusters including γδ T cells, T<sub>reg</sub> cells and distinct differentiation stages of CD4<sup>+</sup> and CD8<sup>+</sup> T cells (Fig. 3a). Concomitant with the reduced tumor growth

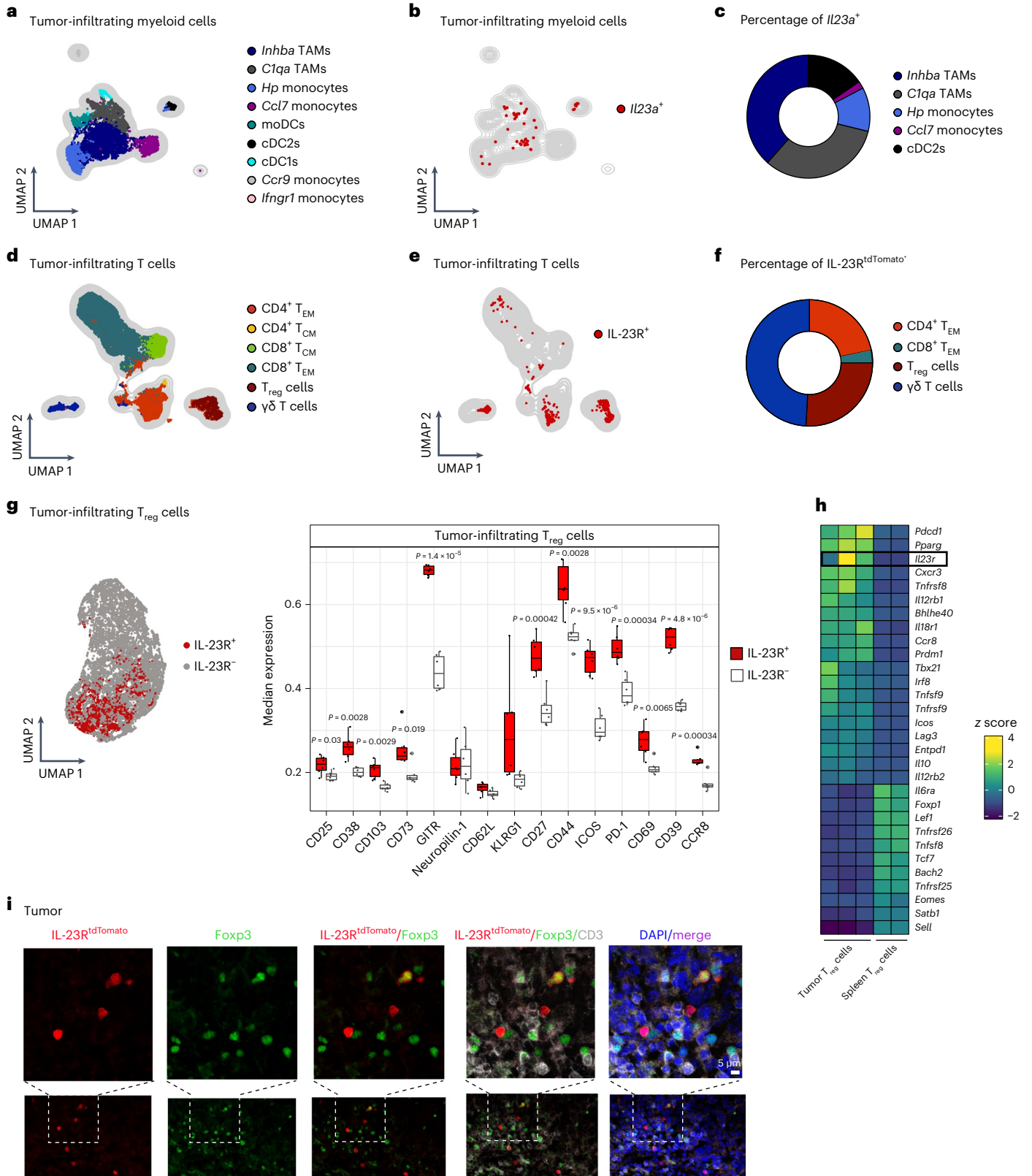
#### Fig. 1 | IL-23R marks a highly suppressive T<sub>reg</sub> cell subset in the mouse TME.

**a–c**, Analysis of a myeloid cell scRNA-seq dataset from mouse B16 tumors<sup>18</sup> (GSE188548; WT tumor). **a**, UMAP depicting tumor-infiltrating myeloid cell clusters. **b**, UMAP displaying *Il23a*<sup>+</sup> myeloid cells. **c**, Pie chart displaying the frequencies of myeloid cell subsets among total *Il23a*<sup>+</sup> myeloid cells. **d–g**, *Foxp3*<sup>DTR-GFP</sup>IL-23R<sup>tdTomato</sup> mice were inoculated intradermally (i.d.) with B16 tumors. TILs were analyzed by flow cytometry on day 14. Data are shown from one representative experiment out of two independent experiments with  $n = 5–6$  biologically independent animals. **d**, UMAP with overlaid FlowSOM clustering (gated on CD45<sup>+</sup>TCRβ<sup>+</sup>TCRγδ<sup>+</sup> cells). **e**, UMAP displaying IL-23R<sup>tdTomato</sup><sup>+</sup> T cells. **f**, Pie chart depicting the frequencies of T cell subsets among total IL-23R<sup>tdTomato</sup><sup>+</sup> T cells. **g**, UMAP with overlaid FlowSOM clustering displaying IL-23R<sup>tdTomato</sup><sup>+</sup>Foxp3<sup>+</sup>

and IL-23R<sup>tdTomato</sup><sup>+</sup>Foxp3<sup>+</sup> T<sub>reg</sub> cell clusters (left). Box plots showing median expression of surface markers on IL-23R<sup>+</sup> and IL-23R<sup>-</sup> T<sub>reg</sub> cells are shown on the right. Box plots display the median and interquartile range (IQR; 25–75%), with whiskers representing the upper and lower quartiles ± IQR. Statistical significance was calculated using two-tailed *t*-tests. **h**, Analysis of a bulk next-generation sequencing dataset of T<sub>reg</sub> cells sorted from B16 tumors or spleens (Magnuson et al.<sup>27</sup>). A heat map depicting selected genes among the top 50 DEGs is shown. Expression of *Il23r* is highlighted. **i**, Immunofluorescence stainings of tumors from i.d. inoculated B16 tumor-bearing IL-23R<sup>tdTomato</sup> mice showing Foxp3 (green), IL-23R<sup>tdTomato</sup> (red), CD3 (white), DAPI (blue) and merged signals (purple). Scale bar: 5 μm. Images shown ( $n = 4$ ) are representative of two independent experiments; moDCs, monocyte-derived DCs; T<sub>CM</sub>, central memory T cells.

observed in *Foxp3<sup>Cre-YFP</sup>/Il23r<sup>fl/fl</sup>* mice, we found an increased infiltration of all T cell subsets in *Foxp3<sup>Cre-YFP</sup>/Il23r<sup>fl/fl</sup>* mice compared to in *Il23r<sup>fl/fl</sup>* controls (Fig. 3a,b). We then included a tailored set of markers to profile activation, proliferation and dysfunction of T cells in our high-parametric single-cell phenotyping (Fig. 3a,c). Interestingly, CD8<sup>+</sup> T<sub>EM</sub> cells showed a more cytotoxic (granzyme B) and activated (CD38 and CD27) phenotype in tumors of *Foxp3<sup>Cre-YFP</sup>/Il23r<sup>fl/fl</sup>* mice (Fig. 3c).

Similar observations were made in the MC38 model, where most T cell clusters and granzyme B production in CD8<sup>+</sup> T<sub>EM</sub> and CD4<sup>+</sup> T<sub>EM</sub> cells increased in *Foxp3<sup>Cre-YFP</sup>/Il23r<sup>fl/fl</sup>* mice (Extended Data Fig. 3a–c). Also in YUMMER1.7 tumors, TILs from mice lacking *Il23r* in T<sub>reg</sub> cells, albeit not increased in number (Extended Data Fig. 3d,e), displayed a highly activated signature reflected by the expression of CD44, CD25, CD69 and Ki-67 and the transcription factors TCF-1 and TOX (Extended Data



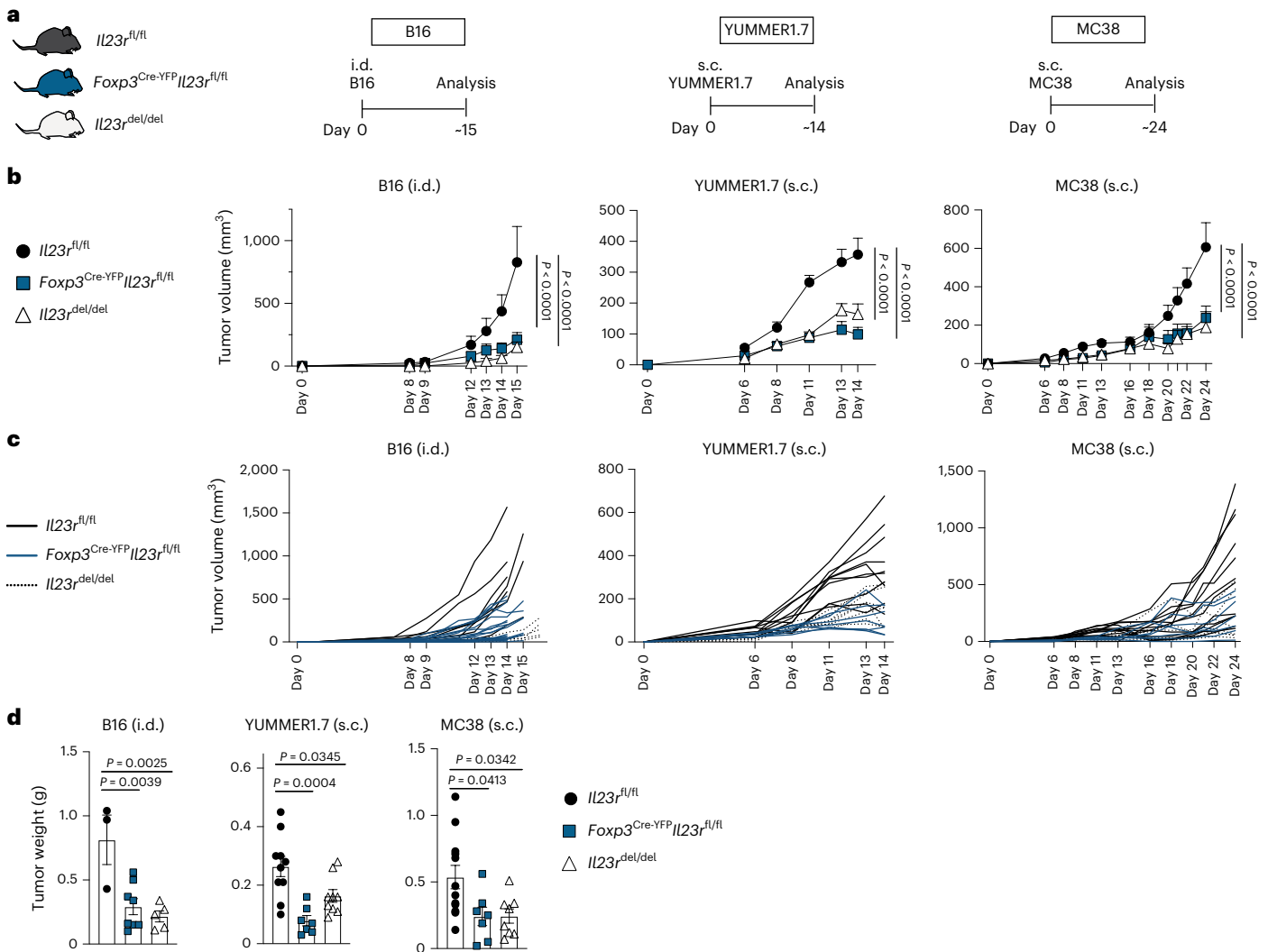


**Fig. 2 | T<sub>reg</sub> cells mediate the tumor-promoting functions of IL-23.** **a–d**, *Il23r<sup>fl/fl</sup>*, *Foxp3<sup>Cre-YFP</sup>Il23r<sup>fl/fl</sup>* and *Il23r<sup>del/del</sup>* mice were inoculated i.d. with B16 tumor cells, inoculated subcutaneously (s.c.) with YUMMER1.7 tumor cells or inoculated s.c. with MC38 tumor cells, and tumors were analyzed around days 15, 14 and 24 after inoculation. The data show the results of three independent experiments (B16:  $n = 3$  *Il23r<sup>fl/fl</sup>* mice,  $n = 5$  *Il23r<sup>del/del</sup>* mice,  $n = 8$  *Foxp3<sup>Cre-YFP</sup>Il23r<sup>fl/fl</sup>* mice; MC38:  $n = 12$  *Il23r<sup>fl/fl</sup>* mice,  $n = 7$  *Foxp3<sup>Cre-YFP</sup>Il23r<sup>fl/fl</sup>* mice,  $n = 7$  *Il23r<sup>del/del</sup>* mice; YUMMER1.7:  $n = 10$  *Il23r<sup>fl/fl</sup>* mice,  $n = 7$  *Foxp3<sup>Cre-YFP</sup>Il23r<sup>fl/fl</sup>* mice,  $n = 8$  *Il23r<sup>del/del</sup>* mice). **a**, Schematic

illustration of the experimental approach. **b**, Tumor volume kinetics of the experimental groups measured by caliper gauge. Data are shown as mean ± s.e.m. Statistical significance was determined by two-way analysis of variance (ANOVA) with a Sidak's post hoc test. **c**, Tumor volume kinetics of individual mice measured by caliper gauge. **d**, Bar graph displaying the final tumor weight. Data are displayed as mean ± s.e.m. Statistical significance was determined using two-tailed t-tests.

Fig. 3f), which mark CD8<sup>+</sup> tumor-specific T cells transitioning toward an intermediate dysfunctional stage<sup>28</sup>.

Next, analyses of tumor-infiltrating myeloid cells of *Foxp3<sup>Cre-YFP</sup>Il23r<sup>fl/fl</sup>* mice and *Foxp3<sup>Cre-YFP</sup>* control mice identified seven distinct clusters, including macrophages, monocyte-derived cells, monocytes, monocyte-derived DCs, DCs, eosinophils and neutrophils (Fig. 3d). The numbers of myeloid subsets remained unchanged after loss of IL-23R in T<sub>reg</sub> cells (Fig. 3e). However, we observed phenotypical changes in macrophages and other myeloid cells in *Foxp3<sup>Cre-YFP</sup>Il23r<sup>fl/fl</sup>* mice (Fig. 3f), marked by reduced levels of arginase-1 and CD206, which are classically linked to immunosuppression and tumor progression<sup>29–31</sup>. By contrast, the expression of proteins enabling enhanced antigen presentation or co-stimulation, such as major histocompatibility complex class II (MHC class II) and CD86, increased (Fig. 3f). Last, we tested how neutralization of IL-23 affected TILs. Albeit less pronounced than in the genetic deletion models, we observed a more activated and less exhausted phenotype marked by higher expression of CD25 on CD4<sup>+</sup> T cells and KLRG1 on CD8<sup>+</sup> T cells, which featured lower PD-1 levels (Extended Data

Fig. 3g). We also observed changes associated with a less suppressive signature in T<sub>reg</sub> cells, denoted by decreased expression of CD38 and PD-1 (Extended Data Fig. 3g).

In summary, we found that IL-23 sensing by T<sub>reg</sub> cells leads to reduced activation of antitumorigenic T effector cells and the induction of immunosuppressive features of myeloid cells.

### IL-23R signaling stabilizes eT<sub>reg</sub> cells

To elucidate the mechanism by which IL-23R signaling in T<sub>reg</sub> cells enhances immunosuppression, we generated *Foxp3<sup>Cre-YFP/+</sup>Il23r<sup>fl/fl</sup>* female mice. In these animals, IL-23R-competent (wild-type (WT)) and IL-23R-deficient T<sub>reg</sub> cells (knockout (KO)) coexist due to stochastic X chromosome inactivation<sup>32</sup>, resulting in a mosaic-like Cre expression, where yellow fluorescent protein (YFP) expression labels *Il23r*-ablated cells (Extended Data Fig. 4a). This was confirmed by quantitative PCR of *Il23r* expression in T<sub>reg</sub> cells (Extended Data Fig. 4b,c).

To explore the dynamics of *Il23r*-KO and WT T<sub>reg</sub> cells, we analyzed tumor-infiltrating and tdLN-derived T<sub>reg</sub> cells on days 9 and 14 after

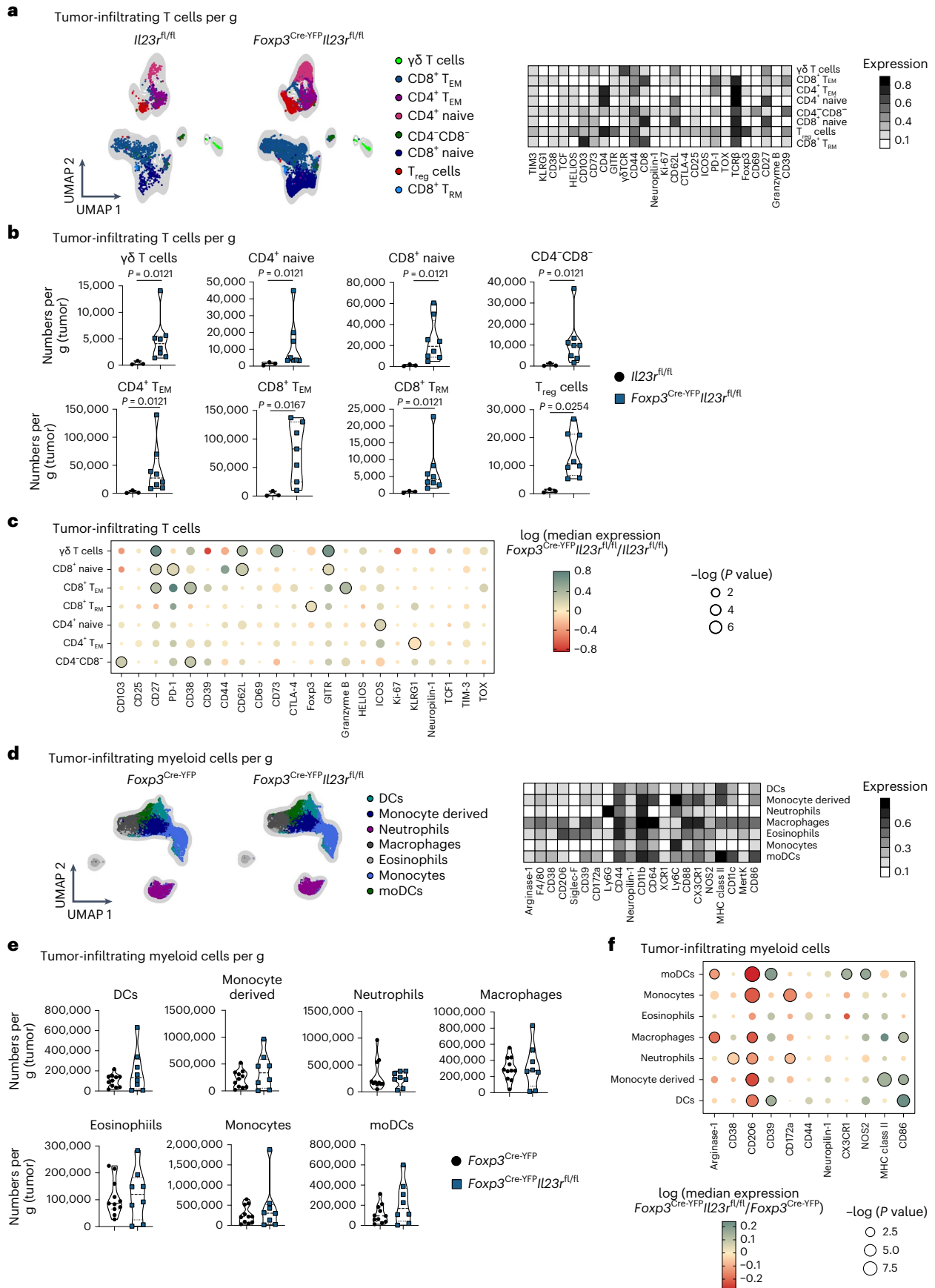


**Fig. 3 | IL-23R signaling in  $T_{reg}$  cells suppresses antitumor immunity.** **a–f**,  $IL23r^{fl/fl}$  and  $Foxp3^{Cre-YFP}IL23r^{fl/fl}$  mice (**a–c**) or  $Foxp3^{Cre-YFP}$  and  $Foxp3^{Cre-YFP}IL23r^{fl/fl}$  mice (**d–f**) were inoculated i.d. with B16 tumor cells, and TILs (gated on CD45<sup>+</sup>TCR  $\beta$ <sup>+</sup>TCR $\gamma\delta$ <sup>+</sup> cells; **a–c**) or myeloid cells (gated on CD45<sup>+</sup>CD90.2<sup>+</sup>CD19<sup>+</sup>NK1.1<sup>+</sup> cells; **d–f**) were analyzed by flow cytometry on day 14 after inoculation. Data are shown from one representative experiment out of two independent experiments with  $n = 3–7$ . **a,d**, UMAP with overlaid FlowSOM clustering (left) and heat map depicting relative marker expression among identified cell clusters (right). **b,e**, Violin plots depicting cell numbers of identified cell clusters per gram (tumor). Data are displayed as mean  $\pm$  s.e.m. Statistical significance was determined using a two-tailed Mann–Whitney  $U$ -test. **c,f**, Dot plot displaying

median marker expression in identified cell clusters comparing  $Foxp3^{Cre-YFP}IL23r^{fl/fl}$  and  $IL23r^{fl/fl}$  (control group) mice (**c**) or  $Foxp3^{Cre-YFP}IL23r^{fl/fl}$  and  $Foxp3^{Cre-YFP}$  (control group) mice (**f**). Statistical significance was determined using two-tailed  $t$ -tests. Color represents log (median expression  $Foxp3^{Cre-YFP}IL23r^{fl/fl}$ /median expression control group); that is, red indicates that median expression is decreased in  $Foxp3^{Cre-YFP}IL23r^{fl/fl}$  mice compared to in the control group, and green indicates that median expression is increased in  $Foxp3^{Cre-YFP}IL23r^{fl/fl}$  mice compared to in the control group. Circle size represents log ( $P$  value). Statistically significant changes ( $P < 0.05$ ) are highlighted with black lines around the circles;  $T_{RM}$ , resident memory T cells.

B16 tumor inoculation (Fig. 4a–f and Extended Data Fig. 4d–h). We found that  $IL23r$ -KO and WT  $T_{reg}$  cells clustered separately (Fig. 4a and Extended Data Fig. 4d).  $IL23r$ -KO  $T_{reg}$  cells accounted for less than 20% of total  $T_{reg}$  cells in tumors (Fig. 4a,b) and less than 30% in tdLNs (Extended Data Fig. 4e) compared to approximately 35% in steady-state LNs and 40% in  $Foxp3^{Cre-YFP/+}$  control mice (Extended Data Fig. 4f,g). This shows that, especially within the TME,  $IL23r$ -KO  $T_{reg}$  cells compete poorly for niche space compared to  $IL23r$ -WT  $T_{reg}$  cells. On day 9 after tumor inoculation, we observed reduced expression of CTLA-4, KLRG1 and ICOS in  $IL23r$ -KO  $T_{reg}$  cells (Fig. 4c). On day 14, the differences between  $IL23r$ -KO and WT  $T_{reg}$  cells further increased, as we found drastically reduced expression of key functional  $T_{reg}$  cell markers (CTLA-4, ICOS, PD-1, CD25 and GITR) as well as tissue homing factors, such as CD62L and CCR8, in  $IL23r$ -KO  $T_{reg}$  cells (Fig. 4c). Further,  $IL23r$ -KO  $T_{reg}$  cells in tumors (Fig. 4c) or tdLNs (Extended Data Fig. 4h) displayed a marked reduction of Foxp3 expression, suggesting loss of  $T_{reg}$  stability. Diminished Foxp3 expression was preceded by a reduction in expression of KLRG1 (a surrogate marker for Blimp-1 reported to stabilize Foxp3 expression<sup>33</sup>) on day 9 (Fig. 4c). Foxp3 expression was equal in YFP<sup>+</sup> and YFP<sup>-</sup>  $T_{reg}$  cells in female  $Foxp3^{Cre-YFP/+}$  control mice (Extended Data Fig. 4i), ruling out an artifactual Cre-mediated effect.

In agreement with previous studies<sup>3</sup>, the vast majority of intratumoral  $T_{reg}$  cells displayed an e $T_{reg}$  phenotype (CD44<sup>+</sup>CD62L<sup>-</sup>; Fig. 4d). By contrast, in the tdLNs, we identified three  $T_{reg}$  differentiation stages, including activated  $T_{reg}$  cells, e $T_{reg}$  cells and naive  $T_{reg}$  cells (Fig. 4d,e). Although the frequencies of  $IL23r$ -KO and WT  $T_{reg}$  cells were almost equal across naive  $T_{reg}$  cells (approximately 40%  $IL23r$  KO and 60% WT), the proportion of  $IL23r$ -KO  $T_{reg}$  cells within the activated and mostly within the e $T_{reg}$  cluster was drastically diminished (approximately 5%  $IL23r$  KO and 95% WT; Fig. 4f). This suggests that e $T_{reg}$  cells in particular depend on IL-23 sensing, which potentially explains the overall lower percentages of  $IL23r$ -KO  $T_{reg}$  cells in tumors where e $T_{reg}$  cells are the dominant  $T_{reg}$  cell subtype<sup>3,4</sup> (Fig. 4b and Extended Data Fig. 4e). As e $T_{reg}$  cells are also prominent in healthy non-lymphoid tissues, we analyzed the levels of IL-23R expression and percentages of e $T_{reg}$  cells of total  $T_{reg}$  cells across different organs using  $Foxp3^{DTR-GFP}IL23R^{tdTomato}$  mice (Fig. 4g,h).

#### Fig. 4 | IL-23R signaling confers a selective advantage on e $T_{reg}$ cells.

**a–f**,  $Foxp3^{Cre-YFP}IL23r^{fl/fl}$  female mice were inoculated i.d. with B16 cells and  $T_{reg}$  cells from tumors, and tdLNs were analyzed by flow cytometry on day 9 or 14 after injection. Data are shown from one representative experiment out of two independent experiments with  $n = 5–6$ . **a**, UMAP and FlowSOM clustering displaying  $T_{reg}$  cell subsets in tumors. **b**, Frequency plots of  $IL23r$ -KO and WT  $T_{reg}$  cells out of total  $T_{reg}$  cells in tumors. **c**, Spiral plot displaying the effect size of differential marker expression between  $IL23r$ -KO and WT  $T_{reg}$  cells in tumors. **d**, Representative contour plots depicting  $T_{reg}$  cells on day 14 after tumor inoculation. **e**, UMAP and FlowSOM clustering displaying  $T_{reg}$  cells in tdLNs on day 14 after tumor inoculation (left). A heat map depicting relative marker expression is shown on the right. **f**, Frequency plots of subsets of  $IL23r$ -KO and WT  $T_{reg}$  cells in tdLNs on day 14 after tumor injection. Statistical significance was determined by two-way ANOVA with a Sidak's post hoc test. **g,h**, Scatter plot (**g**) and violin plots (**h**) displaying frequencies of IL-23R<sup>+</sup>  $T_{reg}$  and e $T_{reg}$  cells among total  $T_{reg}$  cells. Data are pooled from one to two experiments with  $n = 3–5$ . **i**,  $IL23r^{fl/fl}$

We found that high IL-23R expression and high percentages of e $T_{reg}$  cells coincided in tumors and non-lymphoid tissues (steady-state skin and colon), whereas low expression of IL-23R was associated with fewer e $T_{reg}$  cells in lymphoid tissues (steady-state LNs, tdLNs and the thymus; Fig. 4g,h), further supporting that IL-23 sensing induces or maintains e $T_{reg}$  cells in the TME. Also, activation of human  $T_{reg}$  cells by polyclonal in vitro TCR stimulation induced IL-23R expression (Extended Data Fig. 4j).

We then analyzed the expression of effector cytokines (interferon- $\gamma$  (IFN $\gamma$ ), IL-10, tumor necrosis factor (TNF) and IL-17A) in  $T_{reg}$  cells derived from tumors or tdLNs of  $Foxp3^{Cre-YFP}IL23r^{fl/fl}$  and  $IL23r^{fl/fl}$  mice (Fig. 4i and Extended Data Fig. 4k). IL-17A levels remained unchanged in the absence of IL-23 sensing, but IL-23R-deficient  $T_{reg}$  cells showed enhanced expression of IFN $\gamma$  in tumors but not in tdLNs (Fig. 4i and Extended Data Fig. 4k), which may actively contribute to enhanced antitumor immunity. Also, when we cultured  $T_{reg}$  cells under inflammatory conditions (IL-6 and IFN $\gamma$ ), IL-23 stimulation stabilized the expression of Foxp3 and the expansion of total  $T_{reg}$  cells, similar to our observations in vivo (Extended Data Fig. 4l,m). IL-23 stimulation led to enhanced phosphorylation of STAT3 and STAT5 (Extended Data Fig. 4n), which was also observed when  $T_{reg}$  cells were cultured with IL-2 for 5 d and stimulated with IL-23 for 30 min (Extended Data Fig. 4o). Also,  $IL23r$ -KO  $T_{reg}$  cells isolated from lymphoid tissues displayed increased glycolytic rates compared to  $IL23r$ -WT  $T_{reg}$  cells (Fig. 4j,k), which has been ascribed to  $T_{reg}$  cell instability<sup>34–36</sup>. Of note, we found that  $IL23r$ -KO  $T_{reg}$  cells have significantly reduced suppressive capacity compared to their WT counterparts (Fig. 4l,m), and antibody-mediated blockade of IL-23R reduced (albeit less pronounced) the suppressive capacity of  $T_{reg}$  cells (Fig. 4n).

Together, our data indicate that IL-23 confers a selective advantage for e $T_{reg}$  cells and is crucial for  $T_{reg}$  stability and suppressive functions.

#### IL-23R sensing initiates an e $T_{reg}$ program in the murine TME

To identify the downstream effects of IL-23R signaling in  $T_{reg}$  cells, we analyzed pre-enriched CD4<sup>+</sup> T cells isolated from B16 tumors and tdLNs (day 13) of  $Foxp3^{Cre-YFP/+}IL23r^{fl/fl}$  female mice using targeted

and  $Foxp3^{Cre-YFP}IL23r^{fl/fl}$  mice were inoculated i.d. with MC38 tumor cells.  $T_{reg}$  cells were analyzed by flow cytometry on day 14 after inoculation. Violin plots display the median expression (median fluorescence intensity (MFI)) of cytokines. The data shown are from one experiment with  $n = 6–12$ . **j**, Extracellular acidification rate (ECAR) measurement of  $T_{reg}$  cells from spleens and LNs of  $Foxp3^{Cre-YFP}IL23r^{fl/fl}$  or  $Foxp3^{Cre-YFP}$  mice under the specified conditions after stimulation with anti-CD3/anti-CD28, IL-2 and IL-23 for 72 h. Data are representative of the results of two independent experiments with  $n = 4$ . **k**, Quantification of glycolysis in  $IL23r$ -KO and WT  $T_{reg}$  cells. **l–n**, Ex vivo suppression of CellTrace Violet-labeled CD4<sup>+</sup> conventional T ( $T_{con}$ ) cell proliferation by  $IL23r$ -KO and WT  $T_{reg}$  cells (**l** and **m**) or WT  $T_{reg}$  cells  $\pm$  anti-IL-23R (**n**). Data shown are from two independent experiments with  $n = 5$ . Statistical significance was assessed by two-way ANOVA with a Sidak's post hoc test. Data in **f**, **i**, **k**, **l** and **n** are displayed as mean  $\pm$  s.e.m. Statistical significance in **c** and **i–k** was determined using two-tailed  $t$ -tests; 2-DG, 2-deoxyglucose; NS, not significant.





**Fig. 5 | IL-23 sensing by  $T_{reg}$  cells initiates an e $T_{reg}$  cell program in the murine TME.** **a–h**, *Foxp3*<sup>Cre-VFP/+</sup> (heterozygous) *IL23r*<sup>fl/fl</sup> female mice were inoculated i.d. with B16 tumor cells, and a combined transcriptome (scRNA-seq) and protein expression analysis of sorted CD4<sup>+</sup> T cells was performed on day 13 after inoculation. Data are shown from one experiment with  $n = 6$ . **a**, UMAP displaying identified tumor-infiltrating  $T_{reg}$  cell clusters (transcriptome; left) and UMAP highlighting *IL23r*-KO and WT  $T_{reg}$  cells (right). **b**, Heat maps showing adjusted  $P$  value (top), average  $\log_2$  (fold change) ( $\log_2$  (FC)); middle) and mean expression (bottom) of subset markers in the identified  $T_{reg}$  cell clusters assessed by Wilcoxon rank-sum test and Benjamini–Hochberg correction. The complete list is available in Supplementary Table 1. **c**, UMAP displaying identified clusters of integrated tumor-infiltrating and tdLN-derived  $T_{reg}$  cells. **d**, UMAP of tdLN and tumor  $T_{reg}$  cells with overlaid pseudotime and principal graph lines calculated with Monocle 3. **e**, Violin plot (left) and UMAP (right) comparing the distribution

of WT and *IL23r*-KO  $T_{reg}$  cells along pseudotime (corresponding to **d**). **f**, Neighborhood graph of DA testing results (left). Coloring indicates  $\log$  (fold change) of differentially abundant neighborhoods between WT and *IL23r*-KO  $T_{reg}$  cells. White neighborhoods are not differentially abundant (false discovery rate of 10%). Dot size corresponds to the number of cells per neighborhood, and edges indicate the number of overlapping cells between neighborhoods. The index cell position in UMAP space (**a**) determines ordering of the neighborhood nodes. The Beeswarm plot (right) indicates the distribution of differentially abundant neighborhoods across clustering-based  $T_{reg}$  cell subsets. **g**, Violin plots depicting the normalized *Foxp3* RNA abundance among identified  $T_{reg}$  cell subsets. **h**, Dot plot displaying selected DEGs between identified  $T_{reg}$  cell subsets encoding transcription factors/signaling proteins (left) and surface or secreted proteins (right). The complete list is available in Supplementary Table 2; c $T_{reg}$ , central  $T_{reg}$  cells.

Fig. 5f). As expected<sup>37</sup>, tumors were enriched for both e $T_{reg}$  cell clusters. Conversely, tdLNs contained more central  $T_{reg}$  cells, including a KO-specific central  $T_{reg}$  cell cluster. Trajectory inference analysis confirmed that tumor-infiltrating e $T_{reg}$  cells represented the most differentiated state (Fig. 5d). Strikingly, we found that *IL23r*-KO  $T_{reg}$  cells had a profound reduction in the proportion of e $T_{reg}$  cells compared to WT cells (Fig. 5e and Extended Data Fig. 5g,h). Mapping the signature of intratumoral *IL23r*-KO  $T_{reg}$  cells along a gradient from activated to e $T_{reg}$  cells further revealed that *IL23r*-KO  $T_{reg}$  cells differ from e $T_{reg}$  cells, suggesting that the differentiation to an e $T_{reg}$  stage requires IL-23R signaling (Extended Data Fig. 5i).

Assigning single cells to partially overlapping neighborhoods on a  $k$ -nearest neighbor graph<sup>38</sup>, which allows for differential abundance (DA) testing of graph neighborhoods, revealed that WT and *IL23r*-KO  $T_{reg}$  cells indeed form distinct cellular states (Fig. 5f and Extended Data Fig. 6a). By superimposing the DA results to the single-cell embedding, we found that the mostly differing neighborhoods of *IL23r*-WT  $T_{reg}$  cells located to the e $T_{reg}$ , activated and proliferating  $T_{reg}$  cell clusters, as opposed to *IL23r*-KO  $T_{reg}$  cells, which showed no enrichment in these clusters (Fig. 5f and Extended Data Fig. 6a).

The evaluation of the differentially expressed genes (DEGs) between intratumoral  $T_{reg}$  cell subsets (Supplementary Table 2) confirmed a marked reduction of *Foxp3* expression in *IL23r*-KO  $T_{reg}$  cells (Fig. 5g). This was accompanied by a decrease in *Prdm1* (encoding Blimp-1) expression in both *IL23r*-KO  $T_{reg}$  cell subsets and an increase in expression of *Dnmt3a* in the *IL23r*-KO  $T_{reg}$  cell 2 subset. In addition, the *IL23r*-KO  $T_{reg}$  cell 2 subset showed increased expression of *Ifng*, *Csf2*, *Tbx21* and *Ybx3* (Fig. 5h and Extended Data Fig. 5f), previously associated with  $T_{reg}$  cell destabilization<sup>39</sup>. Both *IL23r*-KO  $T_{reg}$  cell clusters featured enhanced expression of *Rora*, *Stat3*, *Stat4*, *Stat5a* and *Stat6*, profound changes in the expression of genes encoding chemokine receptors (*Ccr2*, *Ccr5*, *Ccr6*, *Cxcr3* and *Ccr7*; Fig. 5h and Extended Data Fig. 5d) and a marked reduction in the expression of *Klrg1*, which was confirmed at the protein level (Extended Data Fig. 6b). In line with this finding, we found that the highest density of cells expressing *Prdm1*, *Klrg1* and *Gzmb* located to WT *IL23r*  $T_{reg}$  cell clusters, in contrast to *Ifng*, which showed the highest density in *IL23r*-KO  $T_{reg}$  cells (Extended Data Fig. 6c).

In summary, our data demonstrate that IL-23R signaling in mouse  $T_{reg}$  cells stabilizes their differentiation to an e $T_{reg}$  state with enhanced function and stability.

### IL-23R signaling induces an e $T_{reg}$ program in the human TME

To assess the translational value of our findings in the context of human cancer, we analyzed three bulk and scRNA-seq datasets<sup>27,40,41</sup> (Fig. 6 and Extended Data Figs. 7 and 8). In agreement with our data above, we found that TAMs were the main source of *IL23A* (encoding IL-23p19) across multiple human cancer entities<sup>41</sup> (Extended Data Fig. 7a–c).

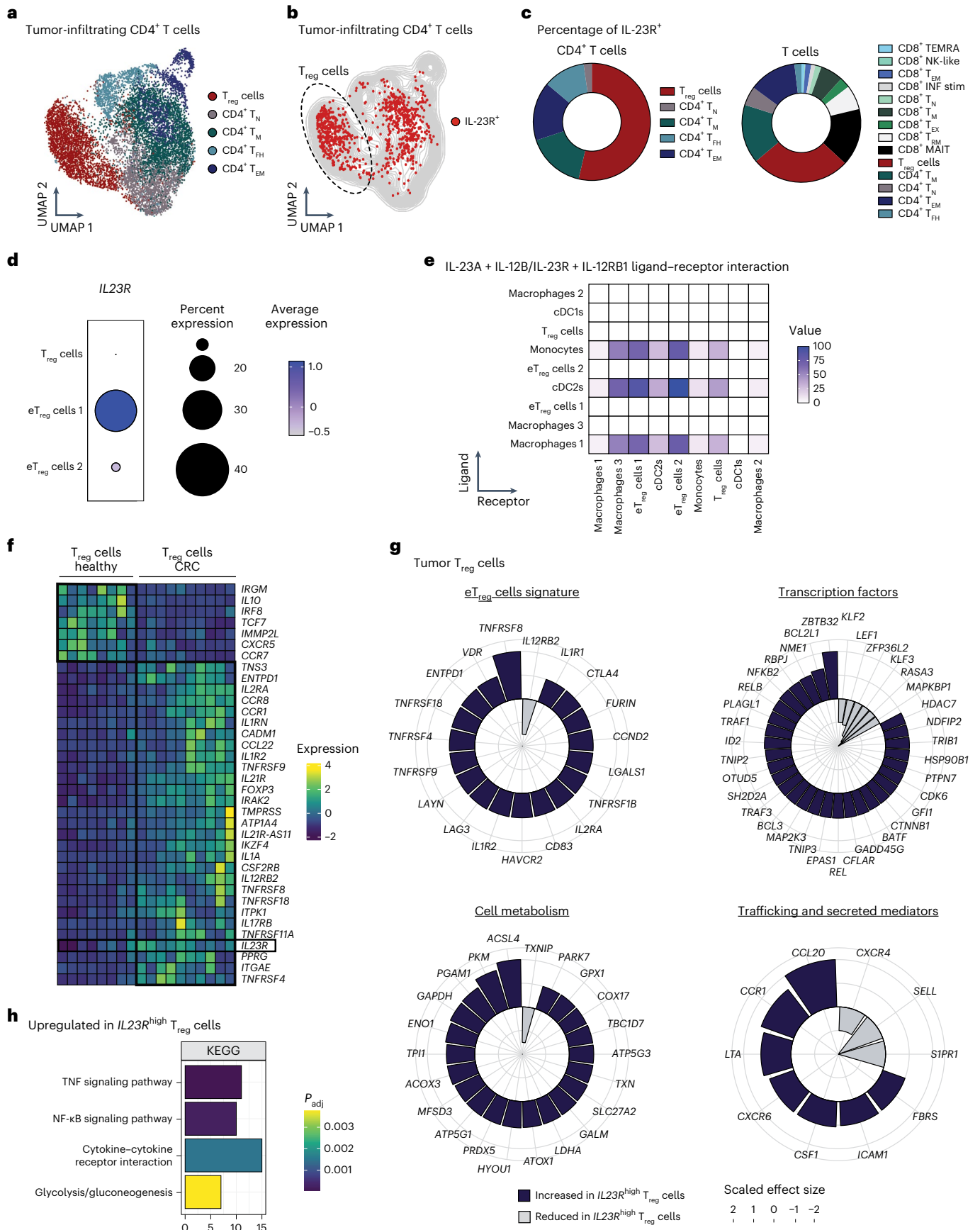
To characterize *IL23R* expression in the TME at the single-cell level, we analyzed an scRNA-seq T cell atlas including 21 malignant entities from 316 individuals<sup>41</sup> (Fig. 6a–c and Extended Data Fig. 7d–h). We assigned eight CD8<sup>+</sup> and five CD4<sup>+</sup> T cell clusters including a  $T_{reg}$  cell cluster (Fig. 6a and Extended Data Fig. 7e–h). Several CD4<sup>+</sup> T cell clusters expressed *IL23R*, including CD4<sup>+</sup> memory T cells,  $T_{EM}$  cells and follicular helper T cells (Fig. 6b,c), whereas CD8<sup>+</sup> mucosal-associated invariant T cells, CD8<sup>+</sup> resident memory T cells and CD8<sup>+</sup> memory T cells were identified as the main *IL23R*-expressing CD8<sup>+</sup> T cell clusters (Fig. 6c).  $T_{reg}$  cells represented the main *IL23R*-expressing cancer T cell cluster, accounting for over 50% of the *IL23R*<sup>+</sup>CD4<sup>+</sup> T cells (Fig. 6b,c) and 29% of total *IL23R*<sup>+</sup> pan-cancer T cells (Fig. 6c). *IL23R*-expressing  $T_{reg}$  cells could be identified across a wide variety of human cancer entities (Extended Data Fig. 7d).

To discern the cross-talk between  $T_{reg}$  cells and myeloid cells within the TME, we performed cell–cell communication analysis<sup>42</sup> on an scRNA-seq dataset of colorectal cancer tissue<sup>43</sup> (Fig. 6d,e and Extended Data Fig. 7i,j). Among the three identified  $T_{reg}$  cell clusters, two displayed an e $T_{reg}$  gene signature and higher expression of *IL23R* than the less activated  $T_{reg}$  cell cluster resembling that of peripheral blood  $T_{reg}$  cells (Fig. 6d)<sup>43</sup>. Among myeloid cells, we identified cDC1s, cDC2s, monocytes and three macrophage subsets<sup>44,45</sup>. Cell–cell communication analysis revealed highly predicted ligand–receptor interactions via the IL-23A + IL-12B/IL-23R + IL-12RB1 axis between myeloid cells (macrophage cluster 1, monocytes and cDC2s) and e $T_{reg}$  cells (Fig. 6e), which was among the top 25 predicted interactions (Extended Data Fig. 8a–c).

### Fig. 6 | IL-23R signaling induces an e $T_{reg}$ cell program in the human TME.

**a–c**, **g**, **h**, Analyses of a human pan-cancer single-cell sequencing dataset<sup>41</sup>. **a**, UMAP displaying pan-cancer CD4<sup>+</sup> T cells. **b**, UMAP highlighting *IL23R*<sup>+</sup>CD4<sup>+</sup> T cells. **c**, Pie chart depicting the frequencies of T cell subsets among total *IL23R*<sup>+</sup>CD4<sup>+</sup> T cells (left) and among total *IL23R*<sup>+</sup> T cells (right). **d**, **e**, Analysis of an scRNA-seq dataset of human colorectal carcinomas (Liu et al.<sup>43</sup>). **d**, Dot plot displaying *IL23R* expression across  $T_{reg}$  cell subsets. **e**, Interaction heat map based on inferred ligand–receptor score between myeloid and  $T_{reg}$  cell subsets of the IL-23A + IL-12B/IL-23R + IL-12RB1 axis computed with ICELLNET. The intensity of communication score is depicted as color intensity value. **f**, Heat map depicting the median expression of selected genes among the top 50 DEGs between  $T_{reg}$  cells isolated from healthy colon biopsies and from tumor tissue of individuals

with colorectal cancer from a bulk next-generation sequencing dataset (Magnuson et al.<sup>27</sup>). Expression of *IL23R* is highlighted. **g**, Spiral plots displaying the scaled (positive values between 1 and 2; negative values between –1 and –2) effect size of selected DEGs between *IL23R*<sup>high</sup> (*IL23R* expression > 0) and *IL23R*<sup>low</sup> (*IL23R* expression = 0)  $T_{reg}$  cells. The complete list of DEGs is available in Supplementary Table 3. **h**, Selected significantly enriched pathways from KEGG pathway analysis using G:Profiler comparing *IL23R*<sup>high</sup> and *IL23R*<sup>low</sup>  $T_{reg}$  cells. Significance was calculated by g:GOST using a Fisher's one-tailed test. No downregulated pathways were detected. The complete list is available in Supplementary Table 4;  $T_N$ , naive T cells;  $T_{EX}$ , exhausted T cells;  $T_M$ , memory T cells;  $T_{FH}$ , follicular helper T cells; MAIT, mucosal-associated invariant T cells;  $P_{adj}$ , adjusted  $P$  value.



In bulk RNA-seq data comparing  $T_{reg}$  cells from healthy colon biopsies and tumor tissue from individuals with colorectal cancer<sup>27</sup> (Fig. 6f and Extended Data Fig. 8d), we found elevated *IL23R* expression in tumor  $T_{reg}$  cells, which coincided with increased expression of *FOXP3* and its target genes *IL2RA*, *IKZF4*, *ENTPD1* (encoding CD39) and *TNFRSF18* (encoding GITR; Fig. 6f).

To pinpoint how IL-23R signaling shapes  $T_{reg}$  cells at the single-cell level, we next compared the gene expression profile of *IL23R*<sup>high</sup> and *IL23R*<sup>low</sup> pan-cancer  $T_{reg}$  cells from 21 different entities<sup>41</sup> (Fig. 6g,h). We found 216 DEGs (Supplementary Table 3), which we categorized into genes related to the 'e $T_{reg}$  signature', 'transcription factors', 'cell metabolism' and ' $T_{reg}$  cell trafficking and secreted mediators' (Fig. 6g and Supplementary Table 3). We additionally identified IL-23-induced pathways in  $T_{reg}$  cells<sup>46,47</sup> (Fig. 6h and Supplementary Table 4). *IL23R*<sup>high</sup>  $T_{reg}$  cells showed an e $T_{reg}$  gene expression profile<sup>48,49</sup> marked by higher expression of *TNFRSF8* (encoding CD30), *VDR*, *ENTPD1* (encoding CD39), *TNFRSF18* (encoding GITR), *TNFRSF4* (encoding OX-40), *TNFRSF9* (encoding 41-BB), *LAYN*, *LAG3*, *ILIRN*, *ILIR2*, *HAVCR2* (encoding TIM-3), *IL2RA* (encoding CD25), *CTLA-4* and others (Fig. 6g). In line with the increased expression of several TNFRSFs and cytokine receptors, TNF signaling and cytokine/cytokine receptor interaction pathways were enriched in *IL23R*<sup>high</sup>  $T_{reg}$  cells (Fig. 6h). Of note, the expression of *IL12RB2* was reduced in *IL23R*<sup>high</sup>  $T_{reg}$  cells (Fig. 6g).

IL-23-sensing  $T_{reg}$  cells showed marked expression of *BATF*, *PLAGL1*, *SH2D2A*, *ZFP36L2*, *NDFIP2* and *CFLAR* (Fig. 6g)<sup>50</sup>. Also, the NF- $\kappa$ B signaling pathway (Fig. 6h) and its associated genes, including *NFKB2* and *REL* (encoding Rel-c), as well as genes encoding trafficking and secreted molecules (*CCR1*, *CXCR6*, *ICAM-1*, *SIPRI*, *SELL* (encoding L-selectin), *CXCR4*, *CCL20*, *LTA*, *CSF1* and *FBSR*) were elevated in expression in *IL23R*<sup>high</sup>  $T_{reg}$  cells (Fig. 6g).

Overarchingly, we observed a trend toward higher *FOXP3* expression in *IL23R*<sup>high</sup>  $T_{reg}$  cells in both the pan-cancer T cell atlas and in a separate single-cell transcriptome dataset from individuals with colorectal cancer<sup>43</sup> (Extended Data Fig. 8e). *IL23R*<sup>high</sup>  $T_{reg}$  cells also displayed a distinct metabolic profile (Fig. 6g).

Together, these data indicate that IL-23R signaling in  $T_{reg}$  cells is a prominent feature across human cancers, promoting a highly suppressive e $T_{reg}$  cell signature<sup>49</sup>.

## Discussion

Here, we identified a crucial role for IL-23R signaling in stabilizing an effector  $T_{reg}$  cell program in the TME. Thus far, identifying IL-23R-expressing cells has been challenging due to the poor specificity of available antibodies and low expression of IL-23R. Nevertheless, two reports have suggested that  $T_{reg}$  cells express IL-23R in preclinical models of cancer<sup>14,22</sup>. By generating an IL-23R reporter mouse, we demonstrated IL-23R expression in  $T_{reg}$  cells in the TME. Although we found that other T cell subsets express IL-23R, specific ablation of *IL23r* in  $T_{reg}$  cells resulted in reduced tumor growth, phenocopying full *IL23r*-KO mice.

TAMs are the predominant IL-23 source in the mouse and human TME, and ligand–receptor interaction analyses consequently indicated potential interactions between these myeloid cells and  $T_{reg}$  cells. It is well established that  $T_{reg}$  cells mediate some of their suppressive functions via antigen-presenting cells through a variety of mechanisms, including the theft of CD80/CD86 via CTLA-4 (refs. 51,52), the depletion of MHC class II<sup>53</sup> or the reprogramming of macrophages toward an anti-inflammatory phenotype<sup>54</sup>. Along this line, we found an increase in CD86 and MHC class II and a decrease in CD206 in several myeloid subsets from tumors where  $T_{reg}$  cells cannot sense IL-23. We thus propose that likely not only one but several mechanisms may be responsible for the myeloid cell reprogramming observed in *Foxp3*<sup>Cre-YFP</sup> *IL23r*<sup>fl/fl</sup> mice.

In line with previous observations<sup>14,15,17</sup>, we found an expansion of effector T cells and  $T_{reg}$  cells in the  $T_{reg}$  cell-specific *IL23r*-KO mouse strain in two tumor models. Of note, the activation status of (non- $T_{reg}$ )

TILs showed some model-specific variations, which may be explained by differences in the degree of immunogenicity, growth kinetics and time points of analysis. Nonetheless, the overall phenotype, including enhanced activation and effector function, was maintained across all models analyzed. Some differences observed when comparing tumors from *Foxp3*<sup>Cre-YFP</sup> *IL23r*<sup>fl/fl</sup> and control mice might stem from the distinctive inflammatory milieu found in tumors of vastly different sizes. We circumvented this problem using female *Foxp3*<sup>Cre-YFP/+</sup> *IL23r*<sup>fl/fl</sup> mice, which allowed us to compare *IL23r*-KO and WT  $T_{reg}$  cells within the same tumor. When coexisting in the same TME, *IL23r*-KO  $T_{reg}$  cells displayed reduced expression of Foxp3 compared to WT  $T_{reg}$  cells, which was preceded by a decrease in the expression of KLRG1, a surrogate marker for Blimp-1. We hypothesize that Blimp-1 can be induced by IL-23, preventing Foxp3 methylation and thus stabilizing  $T_{reg}$  cell identity within the TME<sup>33</sup>. Indeed, *IL23r*-KO  $T_{reg}$  cells exhibited a reduction in the expression of *Prdm1* (encoding Blimp-1) and an increase in the expression of *Dntm3a*, which has been shown to methylate Foxp3 at the CNS2 region, thereby contributing to  $T_{reg}$  cell destabilization<sup>55</sup>. Furthermore, the genetic signature of Blimp-1-competent compared to Blimp-1-deficient  $T_{reg}$  cells is reminiscent of the impact of IL-23 on  $T_{reg}$  cells<sup>56</sup>.

Further indicative of their instability,  $T_{reg}$  cells lacking *IL23r* showed halted differentiation to late e $T_{reg}$  cell stages and a high expression of IFN $\gamma$ , which is usually suppressed via the Foxp3–Runx1 axis in  $T_{reg}$  cells<sup>57</sup>. Of note, IFN $\gamma$  production by  $T_{reg}$  cells has recently been associated with a defective e $T_{reg}$  cell program<sup>58</sup>, and IL-23R-deficient  $T_{reg}$  cells may directly promote antitumor responses via enhanced IFN $\gamma$  production. Further supporting the notion that IL-23 stabilizes  $T_{reg}$  cells, we found increased glycolysis rates in  $T_{reg}$  cells lacking IL-23R. Unconstrained glycolysis, which can be limited by Foxp3, contributes to  $T_{reg}$  cell destabilization<sup>35</sup>. This is consistent with a recent report showing reduced tumor growth in *Foxp3*<sup>Cre-YFP</sup> *IL23r*<sup>fl/fl</sup> mice using the MC38 tumor model<sup>22</sup>. Wight et al. observed increased *Il12rb2* (but not *Il12rb1*) transcripts and IL-12RB2 protein expression in *IL23r*-KO  $T_{reg}$  cells and proposed that lack of *IL23r* in  $T_{reg}$  cells might enhance their sensitivity for IL-12 signaling by increasing the availability of *IL12rb1* to form the IL-12 receptor with *IL12rb2* (ref. 22). Although we also observed increased expression of *Il12rb2* transcripts in *IL23r*-KO  $T_{reg}$  cells, *Il12rb1* transcript expression remained unchanged or was slightly elevated, indicating that enhanced IL-12 responsiveness might be one but not the only mechanism explaining the phenotype of *IL23r*-KO  $T_{reg}$  cells. Overall, our data suggest that IL-23R transmits a fundamental signal to promote e $T_{reg}$  cell function involving Foxp3 and its downstream targets and therefore does not only serve as a decoy mechanism to prevent the formation of the IL-12 receptor. Because in vitro TCR stimulation of  $T_{reg}$  cells was sufficient to induce IL-23R expression, we presume that  $T_{reg}$  cells, after antigen encounter in the TME, undergo initial activation of IL-23R expression. In turn, IL-23 sensing allows the stabilization of the full e $T_{reg}$  phenotype and local suppression of antitumor immunity. Interestingly, *IL23r* was among the most upregulated genes in  $T_{reg}$  cells after loss of Blimp-1 (ref. 56), suggesting a feedback loop that might also explain why only a fraction of e $T_{reg}$  cells expressed IL-23R. Importantly, we could translate our preclinical findings to human cancer. We found that *IL23R*<sup>high</sup>  $T_{reg}$  cells derived from human tumors are marked by higher expression of key genes encoding e $T_{reg}$  cell molecules.

This report reveals an unexpected immunosuppressive property of an otherwise proinflammatory cytokine. In hindsight, it is not surprising that mediators that can cause immunopathology also engage with regulatory elements such as  $T_{reg}$  cells to limit tissue destruction and terminate immune responses. We can speculate that this dichotomy is inherent across other proinflammatory mediators. In the case of IL-1 $\beta$ , this has recently been proposed<sup>59</sup>. Here, this unexpected role of IL-23R signaling in stabilizing  $T_{reg}$  suppressive functions sets the sound base for the therapeutic targeting of  $T_{reg}$  cells through IL-23 or IL-23R blockade to expand the armamentarium of cancer immunotherapy.

## Online content

Any methods, additional references, Nature Portfolio reporting summaries, source data, extended data, supplementary information, acknowledgements, peer review information; details of author contributions and competing interests; and statements of data and code availability are available at <https://doi.org/10.1038/s41590-024-01755-7>.

## References

- Sakaguchi, S. et al. Regulatory T cells and human disease. *Annu. Rev. Immunol.* **38**, 541–566 (2020).
- Rosenblum, M. D., Way, S. S. & Abbas, A. K. Regulatory T cell memory. *Nat. Rev. Immunol.* **16**, 90–101 (2016).
- Tanaka, A. & Sakaguchi, S. Regulatory T cells in cancer immunotherapy. *Cell Res.* **27**, 109–118 (2017).
- Teh, P. P., Vasanthakumar, A. & Kallies, A. Development and function of effector regulatory T cells. *Prog. Mol. Biol. Transl. Sci.* **136**, 155–174 (2015).
- Labani-Motlagh, A., Ashja-Mahdavi, M. & Loskog, A. The tumor microenvironment: a milieu hindering and obstructing antitumor immune responses. *Front. Immunol.* **11**, 940 (2020).
- Iorgulescu, J. B., Braun, D., Oliveira, G., Keskin, D. B. & Wu, C. J. Acquired mechanisms of immune escape in cancer following immunotherapy. *Genome Med.* **10**, 87 (2018).
- Arce Vargas, F. et al. Fc-optimized anti-CD25 depletes tumor-infiltrating regulatory T cells and synergizes with PD-1 blockade to eradicate established tumors. *Immunity* **46**, 577–586 (2017).
- Klages, K. et al. Selective depletion of Foxp3<sup>+</sup> regulatory T cells improves effective therapeutic vaccination against established melanoma. *Cancer Res.* **70**, 7788–7799 (2010).
- Onizuka, S. et al. Tumor rejection by in vivo administration of anti-CD25 (interleukin-2 receptor  $\alpha$ ) monoclonal antibody. *Cancer Res.* **59**, 3128–3133 (1999).
- Ohue, Y. & Nishikawa, H. Regulatory T (T<sub>reg</sub>) cells in cancer: can T<sub>reg</sub> cells be a new therapeutic target?. *Cancer Sci.* **110**, 2080–2089 (2019).
- Tang, C., Chen, S., Qian, H. & Huang, W. Interleukin-23: as a drug target for autoimmune inflammatory diseases. *Immunology* **135**, 112–124 (2012).
- Croxford, A. L., Mair, F. & Becher, B. IL-23: one cytokine in control of autoimmunity. *Eur. J. Immunol.* **42**, 2263–2273 (2012).
- Zwicky, P., Unger, S. & Becher, B. Targeting interleukin-17 in chronic inflammatory disease: a clinical perspective. *J. Exp. Med.* **217**, e20191123 (2020).
- Kortylewski, M. et al. Regulation of the IL-23 and IL-12 balance by Stat3 signaling in the tumor microenvironment. *Cancer Cell* **15**, 114–123 (2009).
- Langowski, J. L. et al. IL-23 promotes tumour incidence and growth. *Nature* **442**, 461–465 (2006).
- Teng, M. W. L. et al. IL-23 suppresses innate immune response independently of IL-17A during carcinogenesis and metastasis. *Proc. Natl Acad. Sci. USA* **107**, 8328–8333 (2010).
- Teng, M. W. L., Von Scheidt, B., Duret, H., Towne, J. E. & Smyth, M. J. Anti-IL-23 monoclonal antibody synergizes in combination with targeted therapies or IL-2 to suppress tumor growth and metastases. *Cancer Res.* **71**, 2077–2086 (2011).
- Mujal, A. M. et al. Holistic characterization of tumor monocyte-to-macrophage differentiation integrates distinct immune phenotypes in kidney cancer. *Cancer Immunol. Res.* **10**, 403–419 (2022).
- Andreatta, M. et al. Interpretation of T cell states from single-cell transcriptomics data using reference atlases. *Nat. Commun.* **12**, 2965 (2021).
- Awasthi, A. et al. IL-23 receptor GFP reporter mice reveal distinct populations of IL-17-producing cells. *J. Immunol.* **182**, 5904–5908 (2009).
- Yoon, J. et al. IL-23 induced in keratinocytes by endogenous TLR4 ligands polarizes dendritic cells to drive IL-22 responses to skin immunization. *J. Exp. Med.* **213**, 2147–2166 (2016).
- Wight, A. E. et al. Antibody-mediated blockade of the IL23 receptor destabilizes intratumoral regulatory T cells and enhances immunotherapy. *Proc. Natl Acad. Sci. USA* **119**, 2200757119 (2022).
- Jones, L. L., Alli, R., Li, B. & Geiger, T. L. Differential T cell cytokine receptivity and not signal quality distinguishes IL-6 and IL-10 signaling during T<sub>H</sub>17 differentiation. *J. Immunol.* **196**, 2973–2985 (2016).
- Malik, S., Want, M. Y. & Awasthi, A. The emerging roles of  $\gamma\delta$  T cells in tissue inflammation in experimental autoimmune encephalomyelitis. *Front. Immunol.* **7**, 14 (2016).
- McInnes, L., Healy, J. & Melville, J. UMAP: uniform manifold approximation and projection for dimension reduction. *J. Open Source Softw.* **3**, 861 (2018).
- Van Gassen, S. et al. FlowSOM: using self-organizing maps for visualization and interpretation of cytometry data. *Cytometry A* **87**, 636–645 (2015).
- Magnuson, A. M. et al. Identification and validation of a tumor-infiltrating T<sub>reg</sub> transcriptional signature conserved across species and tumor types. *Proc. Natl Acad. Sci. USA* **115**, E10672–E10681 (2018).
- Philip, M. & Schietinger, A. CD8<sup>+</sup> T cell differentiation and dysfunction in cancer. *Nat. Rev. Immunol.* **22**, 209–223 (2022).
- Debacker, J. M., Gondry, O., Lahoutte, T., Keyaerts, M. & Huvenne, W. The prognostic value of CD206 in solid malignancies: a systematic review and meta-analysis. *Cancers* **13**, 3422 (2021).
- Ekmekcioglu, S., Grimm, E. A. & Roszik, J. Targeting iNOS to increase efficacy of immunotherapies. *Hum. Vaccin. Immunother.* **13**, 1105–1108 (2017).
- Niu, F. et al. Arginase: an emerging and promising therapeutic target for cancer treatment. *Biomed. Pharmacother.* **149**, 112840 (2022).
- Fontenot, J. D. et al. Regulatory T cell lineage specification by the forkhead transcription factor Foxp3. *Immunity* **22**, 329–341 (2005).
- Garg, G. et al. Blimp1 prevents methylation of Foxp3 and loss of regulatory T cell identity at sites of inflammation. *Cell Rep.* **26**, 1854–1868 (2019).
- Zappasodi, R. et al. CTLA-4 blockade drives loss of T<sub>reg</sub> stability in glycolysis-low tumours. *Nature* **591**, 652–658 (2021).
- Gerriets, V. A. et al. Foxp3 and Toll-like receptor signaling balance T<sub>reg</sub> cell anabolic metabolism for suppression. *Nat. Immunol.* **17**, 1459–1466 (2016).
- Wei, J. et al. Autophagy enforces functional integrity of regulatory T cells by coupling environmental cues and metabolic homeostasis. *Nat. Immunol.* **17**, 277–285 (2016).
- Dixon, M. L., Leavenworth, J. D. & Leavenworth, J. W. Lineage reprogramming of effector regulatory T cells in cancer. *Front. Immunol.* **12**, 717421 (2021).
- Dann, E., Henderson, N. C., Teichmann, S. A., Morgan, M. D. & Marioni, J. C. Differential abundance testing on single-cell data using *k*-nearest neighbor graphs. *Nat. Biotechnol.* **40**, 245–253 (2021).
- Munn, D. H., Sharma, M. D. & Johnson, T. S. T<sub>reg</sub> destabilization and reprogramming: implications for cancer immunotherapy. *Cancer Res.* **78**, 5191–5199 (2018).
- Cheng, S. et al. A pan-cancer single-cell transcriptional atlas of tumor infiltrating myeloid cells. *Cell* **184**, 792–809 (2021).

41. Zheng, L. et al. Pan-cancer single-cell landscape of tumor-infiltrating T cells. *Science* **374**, abe6474 (2021).
42. Noël, F. et al. Dissection of intercellular communication using the transcriptome-based framework ICELLNET. *Nat. Commun.* **12**, 1089 (2021).
43. Liu, Y. et al. Immune phenotypic linkage between colorectal cancer and liver metastasis. *Cancer Cell* **40**, 424–437 (2022).
44. Revel, M., Sautès-Fridman, C., Fridman, W. H. & Roumenina, L. T. C1q<sup>+</sup> macrophages: passengers or drivers of cancer progression. *Trends Cancer* **8**, 517–526 (2022).
45. Hu, J. M. et al. CD163 as a marker of M2 macrophage, contribute to predict aggressiveness and prognosis of Kazakh esophageal squamous cell carcinoma. *Oncotarget* **8**, 21526–21538 (2017).
46. Kanehisa, M., Sato, Y., Kawashima, M., Furumichi, M. & Tanabe, M. KEGG as a reference resource for gene and protein annotation. *Nucleic Acids Res.* **44**, D457–D462 (2016).
47. Reimand, J. et al. g:Profiler—a web server for functional interpretation of gene lists (2016 update). *Nucleic Acids Res.* **44**, W83–W89 (2016).
48. Doebbele, M. et al. CD83 expression is essential for T<sub>reg</sub> cell differentiation and stability. *JCI Insight* **3**, e99712 (2018).
49. Mijnheer, G. et al. Conserved human effector T<sub>reg</sub> cell transcriptomic and epigenetic signature in arthritic joint inflammation. *Nat. Commun.* **12**, 2710 (2021).
50. Alvisi, G. et al. IRF4 instructs effector T<sub>reg</sub> differentiation and immune suppression in human cancer. *J. Clin. Investig.* **130**, 3137–3150 (2020).
51. Qureshi, O. S. et al. Trans-endocytosis of CD80 and CD86: a molecular basis for the cell-extrinsic function of CTLA-4. *Science* **332**, 600–603 (2011).
52. Tekguc, M., Wing, J. B., Osaki, M., Long, J. & Sakaguchi, S. T<sub>reg</sub>-expressed CTLA-4 depletes CD80/CD86 by trogocytosis, releasing free PD-L1 on antigen-presenting cells. *Proc. Natl Acad. Sci. USA* **118**, e2023739118 (2021).
53. Akkaya, B. et al. Regulatory T cells mediate specific suppression by depleting peptide–MHC class II from dendritic cells. *Nat. Immunol.* **20**, 218–231 (2019).
54. Tiemessen, M. M. et al. CD4<sup>+</sup>CD25<sup>+</sup>Foxp3<sup>+</sup> regulatory T cells induce alternative activation of human monocytes/macrophages. *Proc. Natl Acad. Sci. USA* **104**, 19446–19451 (2007).
55. Jain, R. et al. Interleukin-23-induced transcription factor Blimp-1 promotes pathogenicity of T helper 17 cells. *Immunity* **44**, 131–142 (2016).
56. Dixon, M. L. et al. Remodeling of the tumor microenvironment via disrupting Blimp1<sup>+</sup> effector T<sub>reg</sub> activity augments response to anti-PD-1 blockade. *Mol. Cancer* **20**, 150 (2021).
57. Ono, M. et al. Foxp3 controls regulatory T-cell function by interacting with AML1/Runx1. *Nature* **446**, 685–689 (2007).
58. Di Pilato, M. et al. Targeting the CBM complex causes T<sub>reg</sub> cells to prime tumours for immune checkpoint therapy. *Nature* **570**, 112–116 (2019).
59. Mair, F. et al. Extricating human tumour immune alterations from tissue inflammation. *Nature* **605**, 728–735 (2022).

**Publisher's note** Springer Nature remains neutral with regard to jurisdictional claims in published maps and institutional affiliations.

**Open Access** This article is licensed under a Creative Commons Attribution 4.0 International License, which permits use, sharing, adaptation, distribution and reproduction in any medium or format, as long as you give appropriate credit to the original author(s) and the source, provide a link to the Creative Commons license, and indicate if changes were made. The images or other third party material in this article are included in the article's Creative Commons license, unless indicated otherwise in a credit line to the material. If material is not included in the article's Creative Commons license and your intended use is not permitted by statutory regulation or exceeds the permitted use, you will need to obtain permission directly from the copyright holder. To view a copy of this license, visit <http://creativecommons.org/licenses/by/4.0/>.

© The Author(s) 2024

## Methods

### Mice

B6.129(Cg)-*Foxp3*<sup>tm3(DTR/GFP)*Ayr*/J</sup> (*Foxp3*<sup>DTR-GFP</sup>) mice and B6.129(Cg)-*Foxp3*<sup>tm4(YFP/cre)*Ayr*/J</sup> (*Foxp3*<sup>Cre-YFP</sup>) mice were purchased from The Jackson Laboratory (016958 and 016959, respectively). *IL23r*<sup>fl/fl</sup> mice were obtained from P. Rosenstiel, University of Kiel, Germany<sup>60</sup>. *IL23r*<sup>fl/fl</sup> mice were crossed to a Deleter-Cre line CMV (Deleter) Cre (006054) to obtain *IL23r*<sup>del/del</sup> mice. *IL-23R*<sup>tdTomato</sup> mice were generated by M. Oukka, Children's Hospital Seattle, USA and Biocytogen plasmid construction service. Mice were maintained on a C57BL/6 background and were housed in a specific pathogen-free environment. Both female and male mice were used for experiments at the age of 6–10 weeks. Mice were socially housed with a dark/light cycle of 12 h, ambient temperature of 22 °C and 45–65% humidity. All experiments were approved by the Cantonal Veterinary Office of Zurich.

### Mouse tumor models

B16 cells were originally received from Xenogen. The MC38 cell line was received from M. Dettmer, ETH Zurich, Switzerland. The YUMMER1.7 cell line was purchased from Merck-Millipore. Mice were inoculated i.d. with  $1.5 \times 10^5$  B16 cells, s.c. with  $2 \times 10^6$  YUMMER1.7 cells or s.c. with  $3 \times 10^5$  MC38 cells. Starting from day 7 after injection, tumor size and body weight were measured. Measurements were first performed three times a week and later daily. Mice were killed by CO<sub>2</sub> inhalation.

### Tissue processing

Tumors were minced into pieces and digested in RPMI supplemented with 2% fetal calf serum (FCS), 1 mg ml<sup>-1</sup> collagenase IV and 100 µg ml<sup>-1</sup> DNase I (both Sigma-Aldrich) at 37 °C for 45 min. Tissues were then disrupted with a syringe (18-gauge needle) and digested for another 15 min. Cells were then filtered through 100-µm cell strainers and washed with PBS. LNs and thymi were ground through 100-µm cell strainers and washed with PBS. Immune cells were enriched using mouse CD45 TIL microbeads (Miltenyi Biotec) following the manufacturer's instructions.

To digest ear skin, skin was minced into pieces and digested in RPMI supplemented with 2% FCS, 1 mg ml<sup>-1</sup> collagenase IV and 100 µg ml<sup>-1</sup> DNase I (both Sigma-Aldrich) at 37 °C for 1.5 h (ref. 61). Skin tissue was disrupted with a syringe (18-gauge needle) and filtered through 70-µm cell strainers.

To isolate immune cells from mouse colons, 6-cm-long midcolon pieces were washed with cold PBS and incubated in HBSS (without calcium/magnesium) supplemented with 2% FCS, 10 mM HEPES and 5 mM DTT at 80 r.p.m. and 37 °C for 8 min before being incubated three times in HBSS (without calcium/magnesium) supplemented with 2% FCS, 10 mM HEPES and 5 mM EDTA at 80 r.p.m. at 37 °C for 7 min. Next, the colons were rinsed in HBSS (with calcium/magnesium) supplemented with 2% FCS and 10 mM HEPES at 80 r.p.m. at 37 °C for 5 min. Tissues were then minced using a gentleMACS dissociator (Miltenyi Biotec) in digestion buffer (HBSS (with calcium/magnesium) supplemented with 3% FCS, 10 mM HEPES, 30 µg ml<sup>-1</sup> DNase I and 100 µg ml<sup>-1</sup> Liberase and incubated at 120 r.p.m. at 37 °C for 25 min before being filtered through a 100-µm cell strainer and washed with cold PBS.

### Quantitative real-time PCR

RNA from sorted cells was isolated using a Quick-RNA Microprep kit (Zymogen). Reverse transcription of RNA to cDNA was performed using M-MLV reverse transcriptase (Invitrogen). Quantitative real-time PCR was performed on a CFX384 Touch Real-Time PCR Detection System (Bio-Rad) using SYBR Green (Bio-Rad). The following primer pairs were used: *IL23r*: forward CCAAGTATATTGTGCATGTGAAGA, reverse AGCTTGAGGCAAGATATTGTTGT; *Polr2a*: forward CTGGTCCTTCGAATCCGCATC, reverse GCTCGATACCTGCAGGGTCA.

### Flow cytometry

For intracellular cytokine labeling, cells were restimulated in medium containing ionomycin (500 ng ml<sup>-1</sup>; Invitrogen) and phorbol

12-myristate 13-acetate (50 ng ml<sup>-1</sup>; AppliChem; RPMI complete) with GolgiPlug and GolgiStop (both 1:1,000; BD Biosciences) at 37 °C for 4 h. For surface antibodies, single-cell suspensions were incubated with antibodies in PBS at 4 °C for 20 min. For intranuclear/intracellular stainings, cells were fixed and permeabilized using the eBioscience Foxp3/transcription factor fixation/permeabilization concentrate and diluent, 2% buffered formalin or BD Cytofix at 4 °C for 20 to 35 min. Thereafter, cells were incubated with antibodies in permeabilization buffer (BD) at 4 °C for 30 min, 2 h or overnight.

Viability dyes (1:500 dilution) were either purchased from BioLegend (Zombie NIR) or BD Biosciences (LIVE DEAD Blue). Anti-mouse antibodies, including anti-CD279 (BV785, clone 29F.1A12, 1:200 dilution), anti-ICOS (BV750, clone C398.4A, 1:200 dilution), anti-NK1.1 (BV711, clone PK136, 1:150 dilution), anti-CD25 (BV650, clone PC61, 1:100 dilution), anti-CD152 (BV605, clone UC10-4B9, 1:200 dilution), anti-CD62L (BV570, clone MEL-14, 1:200 dilution), anti-granzyme B (Pacific Blue, clone GB11, 1:50 dilution), anti-neuropilin-1 (BV421, clone 3E+12, 1:200 dilution), anti-CD103 (Biotin, clone 2E7, 1:100 dilution), anti-Helios (PE-Cy7, clone 22F6, dilution 1:30), anti-TCRβ (PE-Cy5, clone H57-597, dilution 1:300), anti-KLRG1 (BV421, clone 2F1/KLRG1, dilution 1:200), anti-KLRG1 (PE-Dazzle 594, clone 2F1/KLRG1, dilution 1:400), anti-CD38 (APC-Fire 810, clone 90, dilution 1:400), anti-CCR8 (Spark NIR 685, clone SA214G2, dilution 1:200), anti-TIM-3 (APC, clone RMT3-23, dilution 1:400), anti-TIM-3 (PE-Fire 810, clone RMT3-23, dilution 1:400), anti-CD4 (Spark NIR 685, clone GK1.5, 1:250 dilution), anti-CD206 (Alexa Fluor 700, clone C068C2, dilution 1:600), anti-F4/80 (APC/Fire750, clone BM8, dilution 1:400), anti-CD86 (PE-Dazzle 594, clone GL1, 1:1,200 dilution), anti-I-A/I-E (PE-Cy5, clone M5/114.15.2, 1:2,000 dilution), anti-CD90.2 (Pacific Blue, clone 30-H12, 1:500 dilution), anti-CD11b (BV510, clone M1/70, 1:1,500 dilution), anti-CD64 (BV605, clone X54-57.1, 1:100 dilution), anti-XCR1 (clone ZET, 1:300 dilution), anti-Ly6C (BV711, clone HK1.4, 1:2,000 dilution), anti-CX3CR1 (BV785, clone SA011F11, 1:400 dilution), anti-T-bet (BV711, clone 4B10, 1:50 dilution), anti-IRF4 (Pacific Blue, clone IRF4.3E4, 1:100 dilution), anti-GFP (Alexa Fluor 488, clone FM264G, 1:50 dilution), anti-CD45 (PE-Fire 810, clone S18009F, 1:150 dilution), anti-Ox-40 (APC-Fire750, clone Ox-86, 1:200 dilution), anti-LAG-3 (custom conjugated to NovaFluor Blue 610/70S (dye purchased from Thermo Fisher), clone C9B7W, 1:300 dilution), anti-TNF (BV711, clone MP6-XT22, 1:600 dilution), anti-IL-2 (BV510, clone JES6-5H4, 1:200) and anti-IL-10 (PE-Dazzle 594, clone JES5-16E3, 1:200 dilution), were obtained from BioLegend. Anti-mouse antibodies, including anti-CD69 (BUV395, clone HL2F3, 1:100 dilution), anti-CD4 (BUV496, clone GK1.5, 1:400 dilution), anti-CD357 (BUV563, clone DTA-1, 1:400 dilution), anti-CD304 (BUV661, clone V46-1954, 1:400 dilution), anti-ST2 (BUV737, clone U29-93, 1:200 dilution), anti-CD8a (BUV805, clone 53-6.7, 1:150 dilution), anti-CD73 (BB660 custom conjugate, clone TY/23, 1:200 dilution), anti-Eomes (PE-CF594, clone X4-83, 1:100 dilution), anti-Eos (PE, clone W7-486, 1:200 dilution), anti-CD27 (R718, clone LG.3A10, 1:200 dilution), anti-Ki-67 (BV480, clone B56, 1:200 dilution), anti-CD44 (BUV737, clone IM7, dilution 1:1,200), anti-Ly6G (BUV563, clone 1A8, 1:700 dilution), anti-CD19 (BUV661, clone 1D3, 1:400 dilution), anti-CD45 (BUV395, clone 30-F11, 1:800 dilution), anti-CD172a (BUV395, clone P84, 1:100 dilution), anti-CD88 (BV750, clone 20/70, 1:200 dilution), anti-NK1.1 (BB700, clone PK136, 1:100 dilution), anti-Siglec-F (BB515, clone E50-2440, 1:2,000 dilution), anti-IL-17A (PE, clone TC11-18H10, 1:600 dilution), anti-pSTAT3 (pY705; PE, clone 4/pSTAT3, 1:200 dilution), anti-pSTAT5 (pY694; Pacific Blue, clone 47/Stat5(pY694), 1:50 dilution), BB630 Streptavidin (custom conjugate, 1:200 dilution) and BUV615 Streptavidin (custom conjugate, 1:200 dilution) were purchased from BD Biosciences. Anti-mouse antibodies, including anti-arginase-1 (APC, clone A1ex5, dilution 1:400), anti-CD11c (PE-Cy5.5, clone N418, 1:1,800 dilution), anti-NOS2 (PE-eFluor610, clone CXNFT, 1:800 dilution), anti-MerTK (PE-Cy7, clone DS5MMER, 1:200 dilution), anti-CD39 (PerCP-eFluor 710, clone 24DMS1, 1:400 dilution), anti-Foxp3 (PE-Cy5.5, clone FJK-16s, 1:200 dilution), anti-IFNγ (PE-Cy7,

clone XMGI.2, 1:400 dilution) and anti-IL-22 (APC, clone IL22JOP, 1:200 dilution) were purchased from Thermo Fisher Scientific. Anti-TCF-1 (Alexa Fluor 488, clone C63D9, 1:200 dilution) was obtained from Cell Signaling Technologies. Anti-TOX (PE, clone REA473, 1:200 dilution) was purchased from Miltenyi.

Data were acquired on a 5L Cytex Aurora (Cytex), and data were analyzed using FlowJo software (Tree Star). Cell sorting was performed on a 3L or 5L FACSARIA III (BD). Fluorochrome-conjugated monoclonal antibodies were purchased from BioLegend, BD, Thermo Fisher, Miltenyi or Cell Signaling Technologies. For blocking, TruStain FcX (BioLegend; purified anti-CD16/32 (clone 93)) was used. Cellblox Blocking Buffer (Thermo Fisher Scientific) was used to further minimize nonspecific binding.

### In vitro cytokine stimulation of T<sub>reg</sub> cells

T<sub>reg</sub> cells derived from *Foxp3*<sup>Cre-YFP</sup> mice were isolated using a CD4<sup>+</sup>CD25<sup>+</sup> Regulatory T Cell Isolation kit (Miltenyi) and were cultured in the presence of 2,000 U ml<sup>-1</sup> recombinant IL-2 (Peprotech) and anti-CD3/CD28 beads of the mouse T<sub>reg</sub> cell expansion kit (Miltenyi) with a ratio of two beads per cell. In addition, recombinant mouse IL-6 (50 ng ml<sup>-1</sup>; Peprotech), IFN $\gamma$  (100 ng ml<sup>-1</sup>; Peprotech) and recombinant IL-23 (20 ng ml<sup>-1</sup>; BioLegend) were added, and the cells were cultured for 5 d. For short-term stimulation, T<sub>reg</sub> cells were, after the 5-d expansion, stimulated with recombinant IL-23 (50 ng ml<sup>-1</sup>; BioLegend) for 30 min. Cells were stained with LIVE/DEAD Zombie NIR for 15 min at 4 °C and fixed using 1:1 fixation concentrate and diluent of the Foxp3 transcription factor kit (Thermo Fisher). The cells were then stained intracellularly with antibodies in perm buffer for 30 min at room temperature in the dark.

### In vitro cultivation of human T<sub>reg</sub> cells

T<sub>reg</sub> cells were sorted by FACS from freshly isolated human peripheral blood mononuclear cells (gated on FOXP3<sup>+</sup>CD45<sup>+</sup>CD3<sup>+</sup>CD4<sup>+</sup>CD27<sup>+</sup>CD25<sup>+</sup>CD127<sup>-</sup>) and incubated in T<sub>reg</sub> cell culture medium containing DMEM supplemented with 10% fetal bovine serum, 1 $\times$  penicillin/streptomycin (Gibco), 1 $\times$  MEM vitamin solution (Gibco), 1 mM sodium pyruvate (Gibco), 1 $\times$  MEM non-essential amino acid solution (Gibco), 100 mM HEPES (Gibco), 0.5 mM 2-mercaptoethanol (Gibco), 1 $\times$  GlutaMAX (Gibco), recombinant human IL-2 500 U ml<sup>-1</sup> (Peprotech) and anti-CD3/CD28 stimulation beads (four beads per cell; human T<sub>reg</sub> cell expansion kit; Miltenyi) at 37 °C for 2 d. CD45<sup>+</sup>CD3<sup>+</sup>CD4<sup>+</sup>CD25<sup>+</sup>CD27<sup>+</sup>FOXP3<sup>+</sup> cells were defined as T<sub>reg</sub> cells (human) by flow cytometry.

### Seahorse assay

Mouse T<sub>reg</sub> cells of *Foxp3*<sup>Cre-YFP</sup> *Il23r*<sup>fl/fl</sup> or *Foxp3*<sup>Cre-YFP</sup> mice were isolated from steady-state spleens and LNs by using the mouse T<sub>reg</sub> cell isolation kit according to the manufacturer's protocol (Miltenyi). Purity was above 90% (assessed by flow cytometry). Isolated T<sub>reg</sub> cells were cultured in T<sub>reg</sub> cell culture medium and stimulated using the mouse T<sub>reg</sub> cell expansion kit (Miltenyi) with four beads per cell and 2,000 U ml<sup>-1</sup> recombinant mouse IL-2 (Peprotech) for 3 d. The ECAR of cultured T<sub>reg</sub> cells was measured in a 96-well XFe Extracellular Flux Analyzer (Agilent)<sup>62</sup>. One hundred and fifty thousand T<sub>reg</sub> cells were starved and plated per well in XF medium (non-buffered RPMI-1640 (Agilent) supplemented with 2 mM L-glutamine) at 37 °C for 30 min. The respective wells were treated with recombinant mouse IL-23 (50 ng ml<sup>-1</sup>; Peprotech) in the Seahorse plate 20 min before measurements. ECAR was investigated at the basal level after glucose addition (final concentration of 10 mM) in response to oligomycin (final concentration of 1  $\mu$ M) and after 2-deoxyglucose (final concentration of 50 mM). Glycolysis was calculated as maximum rate measurement before oligomycin injection – last rate measurement before glucose injection.

### In vitro T<sub>reg</sub> cell suppression assay

For in vitro T<sub>reg</sub> suppression assays<sup>63</sup>, red blood cell lysis was performed using RBC lysis buffer (Abcam) on splenocytes of *Foxp3*<sup>Cre-YFP</sup> mice at

room temperature for 2 min. CD4<sup>+</sup> T cells were enriched using a CD4<sup>+</sup> T cell isolation kit (Miltenyi), and T<sub>reg</sub> cells were then purified by FACS. T<sub>reg</sub> cells were cultured and preactivated in vitro in the presence of 2,000 U ml<sup>-1</sup> recombinant IL-2 (Miltenyi) and CD3/CD28 Dynabeads for 3 d (ref. 64) to induce eT<sub>reg</sub> cell differentiation.

Antigen-presenting cells were enriched by depleting CD90.2<sup>+</sup> splenocytes, exposed to 20  $\mu$ g ml<sup>-1</sup> mitomycin C (Sigma) for 30 min at 37 °C and washed five times with PBS. Antigen-presenting cells were plated at 2  $\times$  10<sup>5</sup> cells per well and used for co-stimulation, and 1  $\mu$ g ml<sup>-1</sup> anti-CD3 (clone 17A2) was added for polyclonal TCR activation. CD4<sup>+</sup> T cells were isolated using a naive T cell isolation kit (Miltenyi) and labeled with CellTrace Violet according to the manufacturer's protocol, and 2.5  $\times$  10<sup>4</sup> cells were seeded per well in 96-well plates. T<sub>reg</sub> cells were added at the indicated ratios, and the assay was performed for 72 h. For antibody treatment, 10  $\mu$ g ml<sup>-1</sup> anti-mouse IL-23R (clone 12B2B64) was added. Percent suppression was assessed based on the division index (DI) calculated in FlowJo with the following formula: percent suppression = 100 - (DI<sub>Treg:Tcon ratio</sub>/DI<sub>Tcon alone</sub>)  $\times$  100 (ref. 65).

### In vivo cytokine blockade

Six- to 8-week-old C57BL/6 mice were subcutaneously inoculated with 3  $\times$  10<sup>5</sup> MC38 cells. The mice were randomized to respective treatment groups on day 6 after inoculation and received a total of three injections of 100  $\mu$ g of anti-p19 (clone G23-8, BioXcell) or isotype control (IgG1, clone MOPC-21, BioXcell) every 72 h intraperitoneally.

### Histology

For immunofluorescence stainings, tissues were fixed in 4% paraformaldehyde at 4 °C for 24 h. Tissues were then put into PBS with 30% sucrose at 4 °C for 72 h and embedded in optimal cutting temperature compound. Cut sections were incubated with working solution (PBS supplemented with 1% bovine serum albumin and 0.02% Tween 20) at 4 °C for 30 min. Sections were then incubated with primary antibodies to Foxp3 and tdTomato diluted in working solution at 4 °C overnight. Sections were washed three times with PBS supplemented with 0.01% Tween for 5 min and were incubated with secondary antibodies and DAPI diluted in working solution at 4 °C for 30 min, followed by another round of five wash steps with PBS and 0.01% Tween 20. Image acquisition was performed on a Leica Stellaris 5.

### High-dimensional analysis of flow cytometry data

Raw fcs-files were preprocessed using FlowJo Software. Compensated and pregated cells were imported into RStudio using R (version 4.0/4.2.2) and the flowCore package<sup>66</sup>. Data were transformed using a hyperbolic arcsine (arcsinh) transformation and percentile normalized to obtain expression values between 0 and 1. This was followed by dimensionality reduction using UMAP by applying the umap package in R<sup>25</sup>. Automated clustering and metaclustering were performed with the FlowSOM algorithm<sup>26</sup>. This was followed by expert-guided merging of clusters<sup>67</sup>.

### scRNA-seq

Mouse tumors were digested as described above. CD4<sup>+</sup> and CD8<sup>+</sup> T cell enrichment was then performed using CD4/CD8 (TIL) MicroBeads (Miltenyi Biotec) following the manufacturer's instructions. Enriched cells were labeled with flow cytometry antibodies in PBS at 4 °C for 20 min. After a wash step with PBS supplemented with 2% FCS, cells were labeled with antibody-seq oligonucleotides (BD) and sample tag antibodies to MHC class I (626545 BD Single-Cell Multiplexing Kit) at 4 °C for 45 min in PBS supplemented with 2% FCS. Antibody-seq oligonucleotides, including anti-CD27 (clone LG.3A10), anti-CD4 (clone GK1.5), anti-CD103 (clone 2E7), anti-CD357 (clone DTA-1), anti-CD8a (clone 53-6.7), anti-CD279 (clone RMP1-30), anti-CD44 (clone IM7), anti-CD25 (clone PC6), anti-CD62L (clone MEL-14), anti-CD45RA (clone 14.8), anti-KLRG1 (clone 2F1), anti-ICOS (clone DX-29) and anti-CD38 (clone 90/CD38), were obtained from BD Biosciences.

Cells were then washed three times with PBS supplemented with 2% FCS, and CD45<sup>+</sup>CD90<sup>+</sup>CD4<sup>+</sup> live cells were sorted by FACS into RPMI supplemented with 5% FCS. Sorted CD4<sup>+</sup> T cells were washed once with PBS supplemented with 2% FCS, and six sample tag-labeled samples were multiplexed to obtain a total of 60,000 cells, which were loaded on a BD Rhapsody cartridge. Single-cell isolation was performed with the BD Rhapsody Express Single-Cell Analysis system according to the manufacturer's protocol (BD Biosciences). Targeted cDNA library preparation was conducted with the targeted mRNA and AbSeq amplification kit (BD Biosciences), the BD Rhapsody Immune Response Panel and a complementary custom-designed targeted panel. Size distribution of the cDNA libraries was performed using a D1000 assay on a TapeStation system (Agilent Technologies). Sequencing was performed on a Novaseq S1 (Illumina) by the Functional Genomics Center Zurich.

### scRNA-seq analysis

Raw sequencing reads were uploaded to the SevenBridges analysis platform. For each sample, the BD Rhapsody targeted analysis pipeline (revision 0) was run using a custom amplicon and AbSeq antibody-tag reference. All other app defaults were left unchanged.

Downstream analysis was performed using the Seurat (4.1.0/4.2.0), SingleCellExperiment (version 1.20.0) and scater (version 1.26.1) packages. Cells with <200 or >2,500 genes were excluded from further analysis.

The data were log normalized and scaled and underwent principal component analysis (PCA) based on all features. Subsequently, clustering and UMAP dimensionality reduction was performed based on 30 principal components and a resolution of 1.2. The clusters were then manually assigned based on their differential marker expression. The identified T<sub>reg</sub> cell cluster was subsetted, and log normalization, scaling and PCA were performed on the subsetted data as described above. For differential expression analysis, a non-parametric Wilcoxon rank-sum test was performed. Tumor and tdLN data were integrated via the Seurat v4 pipeline using SelectIntegrationFeatures, FindIntegrationAnchors and IntegrateData, followed by identical processing as described above. For trajectory inference analysis, the integrated Seurat object was converted into a Monocle 3 cell\_data\_set (cnds) object including previous embedding and clustering information. Using learn\_graph and order\_cells, a principal graph was fitted on the data, and the cells were ordered along a pseudotemporal trajectory with an automatic selection of the root node<sup>68–70</sup>.

The AddModuleScore function was used to compute cluster-specific scores. The SCpubr package<sup>71</sup> (version 1.0.4) was used for visualizations of subset markers and cellular state plots. For the cellular state plots, enrichment scores for each cluster were computed using the AddModuleScore function implemented in Seurat based on the 30 most DEGs between the identified T<sub>reg</sub> cell clusters. The do\_CellularStatesPlot function of the SCpubr package was then leveraged to visualize the enrichment scores. DA testing based on partially overlapping graph neighborhoods was performed using the Milo package (version 1.7.0)<sup>38</sup>. Subsetted T<sub>reg</sub> cells were grouped in *IL23r*-KO and WT T<sub>reg</sub> cells based on their expression of *Yfp-cre*, and the Seurat object was converted into a SingleCellExperiment object before the Milo object was generated. A *k*-nearest neighbors graph with 12 reduced dimensions and *k* = 10 for *k*-nearest neighbors refinement was applied. To perform DA testing, a design matrix with *YFP* positivity as a covariate to test for was applied. The built-in visualization functions of Milo were then used to generate DA plots.

Publicly available scRNA-seq datasets were analyzed using the Seurat (4.1.0/4.2.0) package in RStudio. Briefly, if available, clustering of publicly available data was used, and expert-guided merging of clusters was performed in some cases. Otherwise, expert-guided manual cell-type assignment to the unbiased clusters was performed. Differential expression was assessed using the non-parametric Wilcoxon rank-sum test.

Cell–cell communication network inference was performed on myeloid and T<sub>reg</sub> cell subsets extracted with Seurat using the ICELLNET (version 1.00) packages in RStudio<sup>42,72</sup>.

### Bulk RNA-seq analysis

Differential expression analysis on publicly available bulk RNA-seq datasets was performed using the DESeq2 package (version 1.37.4)<sup>73</sup>. Briefly, unnormalized count matrices were imported into RStudio using R version 4.0. Prefiltering of low-count genes was performed by selecting only genes with ten or more reads. A DESeqDataSet object was then generated using the DESeqDataSetFromMatrix() function with design ~ condition (for example, tumor T<sub>reg</sub> cells versus spleen T<sub>reg</sub> cells). Rows with low gene counts (less than five) were removed in the next step. The DESeq function was then applied with default parameters, and the results were filtered for an adjusted *P* value of <0.05 and log<sub>2</sub> (fold change) of >1.5. Consequently, a *z* score was calculated on these genes.

### Quantification and statistical analysis

Statistical significance was determined using GraphPad Prism 8 (GraphPad Software). Two-tailed, unpaired *t*-tests were used to assess differences between two groups. Statistical significance for disease curves was evaluated by two-way ANOVA with Bonferroni's post hoc test. *n* shows the number of biological replicates. Statistical details for each experiment are indicated in the corresponding figure legends.

### Reporting summary

Further information on research design is available in the Nature Portfolio Reporting Summary linked to this article.

### Data availability

scRNA-seq data generated for this study have been deposited in the Gene Expression Omnibus (<https://www.ncbi.nlm.nih.gov/geo/>) under accession number GSE224072. Human TIL data from a pan-cancer T cell atlas are available under the accession number GSE156728. scRNA-seq data from tumor-infiltrating leukocytes from individuals with colorectal cancer are accessible under the accession number GSE164522. Bulk RNA-seq data of mouse and human tumor-infiltrating T<sub>reg</sub> cells are accessible under the accession number GSE116347. Source data are provided with this paper.

### Code availability

Code will be provided upon reasonable request by the corresponding authors.

### References

60. Aden, K. et al. Epithelial IL-23R signaling licenses protective IL-22 responses in intestinal inflammation. *Cell Rep.* **16**, 2208–2218 (2016).
61. Zwicky, P. et al. IL-12 regulates type 3 immunity through interfollicular keratinocytes in psoriasisform inflammation. *Sci. Immunol.* **6**, eabg9012 (2021).
62. Uhl, F. M. et al. Metabolic reprogramming of donor T cells enhances graft-versus-leukemia effects in mice and humans. *Sci. Transl. Med.* **12**, eabb8969 (2020).
63. Overacre-Delgoffe, A. E. et al. Interferon- $\gamma$  drives T<sub>reg</sub> fragility to promote anti-tumor immunity. *Cell* **169**, 1130–1141 (2017).
64. Collison, L. W. & Vignali, D. A. A. in *Regulatory T Cells*, Vol. 707 (eds Kassiotis, G. & Liston, A.) 21–37 (Humana Press, 2011).
65. McMurphy, A. N. & Levings, M. K. Suppression assays with human T regulatory cells: a technical guide. *Eur. J. Immunol.* **42**, 27–34 (2012).
66. Ellis, B., et al. flowCore: flowCore: basic structures for flow cytometry data. R package version 2.12.2. <https://doi.org/10.18129/B9.bioc.flowCore> (2023).

67. Ingelfinger, F. et al. Single-cell profiling of myasthenia gravis identifies a pathogenic T cell signature. *Acta Neuropathol.* **141**, 901–915 (2021).
68. Trapnell, C. et al. The dynamics and regulators of cell fate decisions are revealed by pseudotemporal ordering of single cells. *Nat. Biotechnol.* **32**, 381–386 (2014).
69. Qiu, X. et al. Reversed graph embedding resolves complex single-cell trajectories. *Nat. Methods* **14**, 979–982 (2017).
70. Cao, J. et al. The single-cell transcriptional landscape of mammalian organogenesis. *Nature* **566**, 496–502 (2019).
71. Blanco-Carmona, E. Generating publication ready visualizations for single cell transcriptomics using SCpubr. Preprint at *bioRxiv* <https://doi.org/10.1101/2022.02.28.482303> (2022).
72. Jin, S. et al. Inference and analysis of cell–cell communication using CellChat. *Nat. Commun.* **12**, 1088 (2021).
73. Love, M. I., Huber, W. & Anders, S. Moderated estimation of fold change and dispersion for RNA-seq data with DESeq2. *Genome Biol.* **15**, 550 (2014).

## Acknowledgements

We thank the Cytometry Core Facility (University of Zurich), the Institute of Laboratory Animal Research (University of Zurich) and the Functional Genomics Center Zurich (University of Zurich) for technical support. We thank F. Hartmann (DKFZ), F. Mair (ETH Zurich), P.-C. Ho (University of Lausanne) and K.-C. Kao (University of Lausanne) for mindful discussions. This project has received funding from the Swiss National Science Foundation (733 310030\_170320, 310030\_188450 and CRSII5\_183478 to B.B.; PROOP3\_179775 to S.T.), the medical research center ‘the LOOP’ (B.B.), the cooperative project ‘Skintegrity’ (B.B.), the European Research Council (ERCAdG\_IMPACT; B.B.), the Swiss Cancer League (KFS-4431-02-2018 to S.T. and B.B.), the Sassella Foundation (S.T.), the Vontobel Foundation (S.T.), the Novartis Foundation (S.T.), the Olga Mayenfisch Foundation (S.T.), the Deutsche Forschungsgemeinschaft (Walter-Benjamin Fellowship to T.W., SFB1054-B06 (ID 210592381) to T.K., TRR128-A07 (ID 213904703) to T.K., TRR355 (ID 490846870) to T.K., TRR128-Z02 (ID 213904703) to T.K., TRR274-A01 (ID 408885537) to T.K., SFB-1479 (ID 441891347) to

R.Z., SFB1160 TP B09 to R.Z., individual grant 872/4-1 to R.Z. and EXC 2145 (SyNergy, ID 390857198) to T.K.) and by the Hertie Network of Clinical Neuroscience (to T.K.).

## Author contributions

T.W. and P.Z. designed, performed and analyzed experiments and developed the overall concept of the study. L.R., C.S., M.V., B.M.S.d.M., C.H., T.R., A.S., S.S., A.H., F.I., C.X., D.K., P.H., A.F.d.S., A.M., N.N. and S.K. performed experiments, supported data analysis or helped editing the manuscript. N.K., R.Z., M.O. and T.K. provided conceptual input. S.T. and B.B. developed the overall concept and supervised and financed the study. T.W., P.Z., S.T. and B.B. wrote the manuscript.

## Funding

Open access funding provided by University of Zurich.

## Competing interests

The authors declare no competing interests.

## Additional information

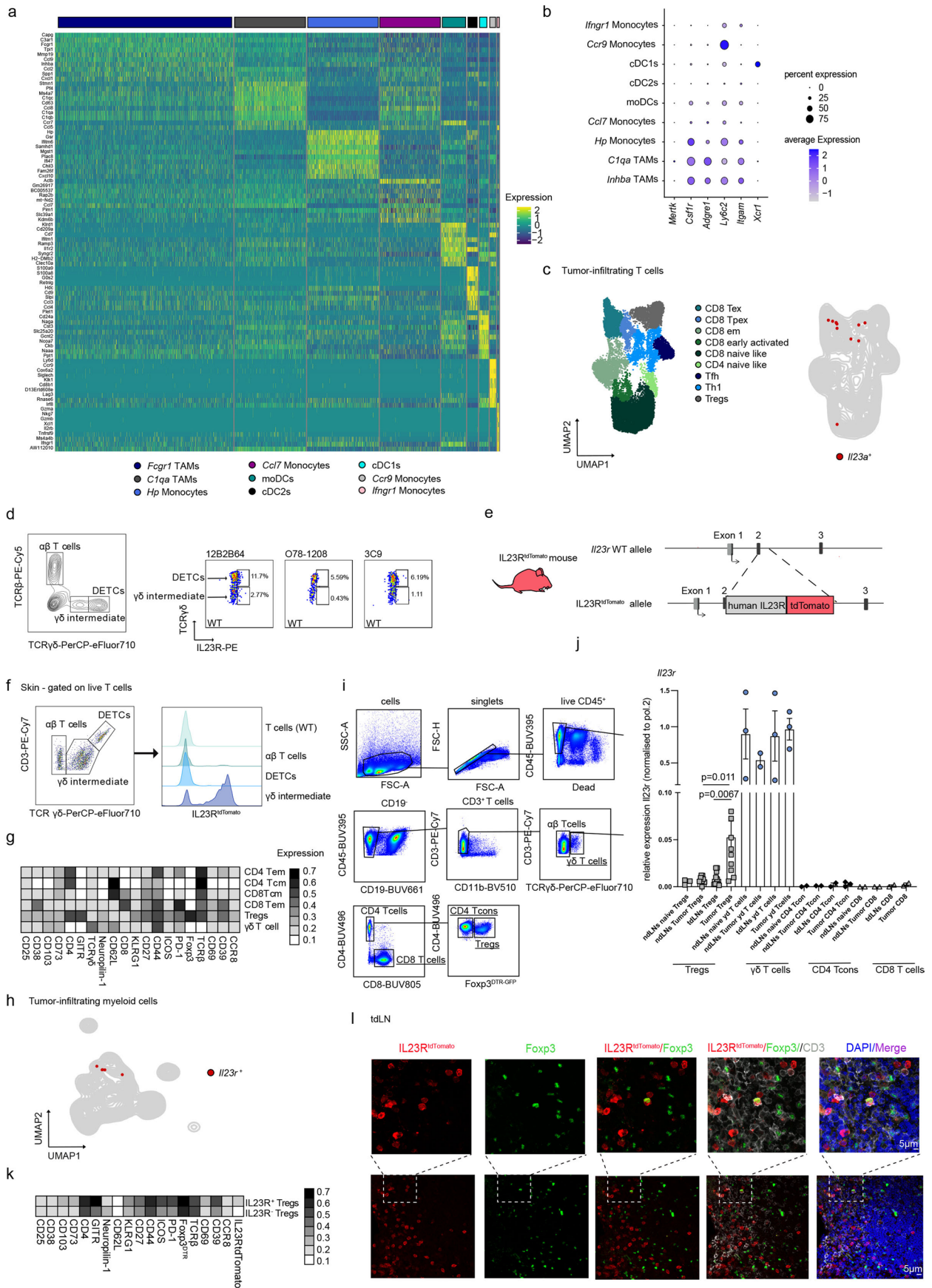
**Extended data** is available for this paper at <https://doi.org/10.1038/s41590-024-01755-7>.

**Supplementary information** The online version contains supplementary material available at <https://doi.org/10.1038/s41590-024-01755-7>.

**Correspondence and requests for materials** should be addressed to Sonia Tugues or Burkhard Becher.

**Peer review information** *Nature Immunology* thanks Vassiliki Boussiatis and the other, anonymous, reviewer(s) for their contribution to the peer review of this work. Primary Handling Editor: S. Houston, in collaboration with the *Nature Immunology* team.

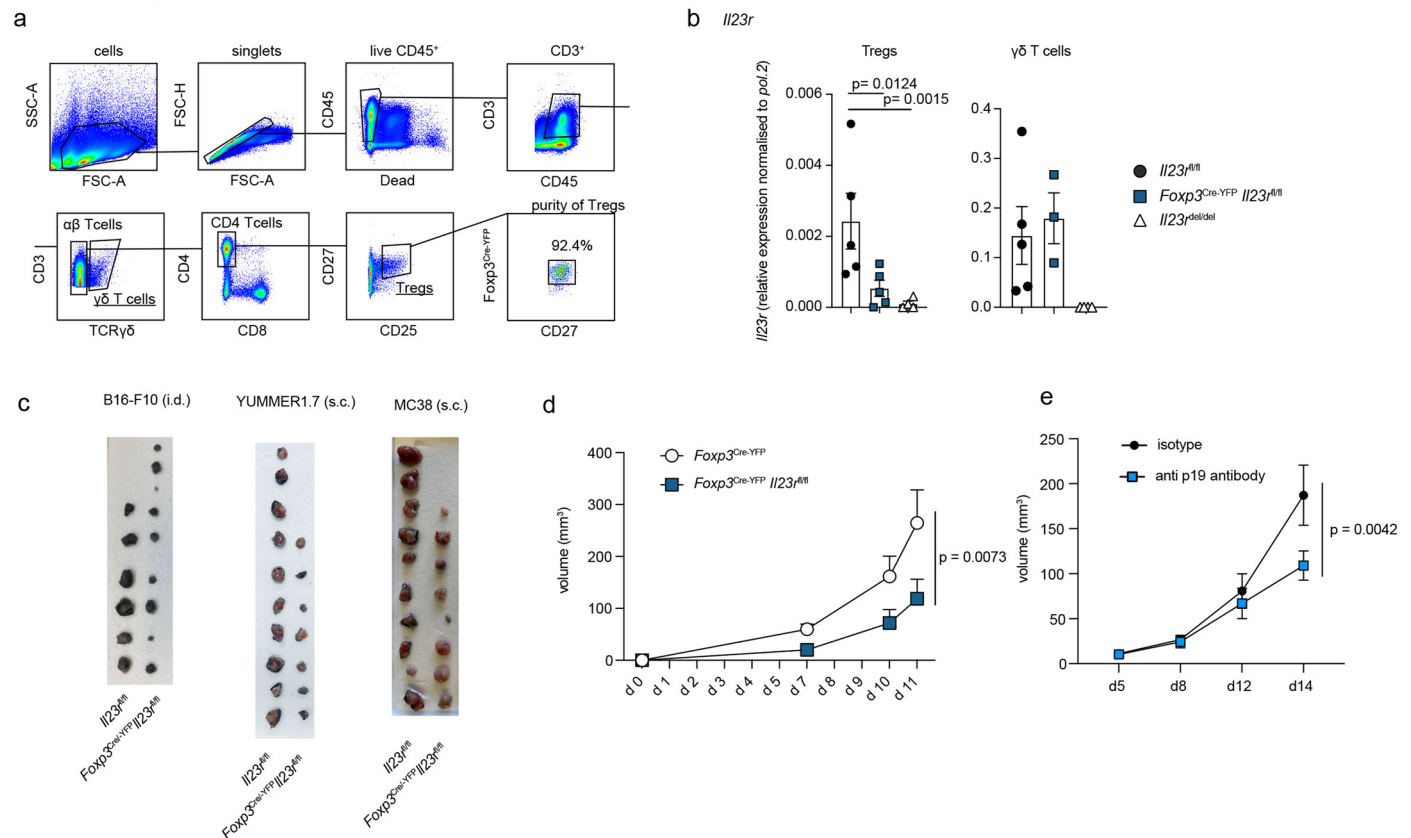
**Reprints and permissions information** is available at [www.nature.com/reprints](http://www.nature.com/reprints).



Extended Data Fig. 1 | See next page for caption.

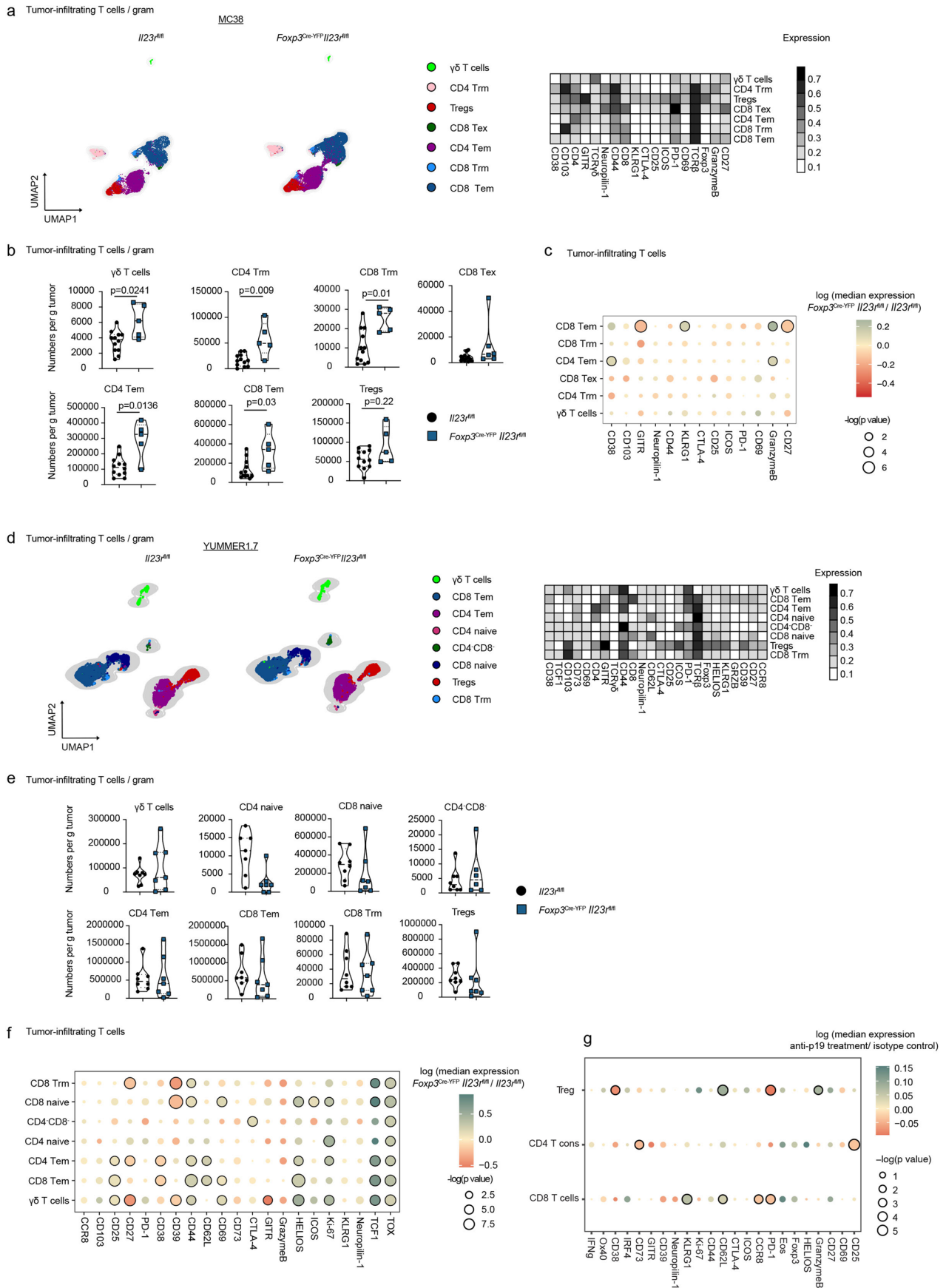
**Extended Data Fig. 1 | IL23R marks a highly suppressive Treg cell subset in the murine TME. (a, b, h)** Myeloid cell-scRNAseq data from murine B16 tumors (Mujal et al. 2022, [GSE188548](#)). **(a)** Heatmap depicting the expression of cell-type-defining genes. **(b)** Dotplot showing the expression of selected lineage markers. **(c)** scRNAseq data of murine pan-tumor T cells (Andreatta et al. 2022, [E-MTAB-9274](#)). UMAP displaying T cell subsets (left) or IL23a<sup>+</sup> T cells (right). **(d)** Representative FACS plot (left) of steady state murine skin CD45<sup>+</sup> cells (left) (pregated on live, CD45<sup>+</sup> cells). Representative FACS plots (right, pregated on live, CD45<sup>+</sup>, TCRγδ<sup>+</sup>) with gates of positive signal of respective IL23R-PE antibody clones of dendritic epidermal T cells (DETCs) (upper gate) and γδ<sup>intermediate</sup> T cells (lower gate). Displayed data are from one experiment with n = 4. **(e)** Schematic illustration of the IL23R<sup>tdTomato</sup> allele. **(f)** Representative FACS plot (left) of murine skin T cells and histograms (right) depicting IL23R<sup>tdTomato</sup> expression among T cell subsets from IL23R<sup>tdTomato</sup> mice and total T cells ('T cells') from WT mice. Data shown from one representative experiment out of two independent experiments with n = 3. **(g, k)** T cells from i.d. inoculated B16 tumors in Foxp3<sup>DTR-GFP</sup> IL23R<sup>tdTomato</sup> mice were analyzed by flow cytometry on day 14. Data shown from

one representative experiment out of two independent experiments with n = 5-6. **(g)** Heatmap displaying marker expression among tumor-infiltrating T cell subsets. **(h)** UMAP displaying IL23r<sup>+</sup> myeloid cells. **(i)** Gating strategy used to FACS-sort γδ, CD8<sup>+</sup>, CD4<sup>+</sup> T cells and Foxp3<sup>+</sup> Treg cells from Foxp3<sup>DTR-GFP</sup> mice. **(j)** Bar graph depicting relative IL23r mRNA expression level (qPCR) in FACS sorted T cells from steady state LNs or tdLNs, ndLNs and tumors from i.d. inoculated B16 tumor-bearing Foxp3<sup>DTR-GFP</sup> mice. Pooled data from three independent experiments. Biologically independent samples: n = 2: ndLNs: γδ T cells, naïve CD4 Tcon; ndLNs: naïve CD8; tdLNs: CD8, CD4 Tcon; Tumor: CD8. n = 3: ndLNs: naïve Treg cell, naïve γδ T cells, γδ T cells; Tumor: γδ T cells, CD4 Tcon. n = 8: ndLNs Tumor Treg cell. n = 10: tdLNs: Treg cell; Tumor: Treg cell. Data are displayed as mean +/- SEM. **(k)** Heatmap displaying relative marker expression among IL23R<sup>+</sup> and IL23R<sup>-</sup> Treg cellclusters. **(l)** Immunofluorescence stainings of tdLNs from i.d. inoculated B16-tumor bearing IL23R<sup>tdTomato</sup> mice. Foxp3 (green), IL23R<sup>tdTomato</sup> (red), CD3 (white) DAPI (blue), merged (purple). Images (n = 4) are representatives from 2 independent experiments.



**Extended Data Fig. 2 | Treg cells mediate the tumor-promoting functions of IL-23.** (a) Gating strategy to FACS sort γδ T cells and Treg cells from LNs of *Foxp3*<sup>Cre-YFP</sup>*Il23r*<sup>fl/fl</sup> and *Il23r*<sup>fl/fl</sup> mice for qPCR and example plot showing purity of sorted Treg cells. (b) Bar graphs depicting relative mRNA expression level of *Il23r* normalized to *pol.2* in FACS sorted γδ T cells and Treg cells from steady state LNs of *Foxp3*<sup>Cre-YFP</sup>*Il23r*<sup>fl/fl</sup>, *Il23r*<sup>fl/fl</sup> and *Il23r*<sup>del/del</sup> mice. Data shown from one representative experiment out of two independent experiments with  $n = 5$  (*Foxp3*<sup>Cre-YFP</sup>*Il23r*<sup>fl/fl</sup> and *Il23r*<sup>fl/fl</sup> mice) or  $n = 3$  (*Il23r*<sup>del/del</sup>) biologically independent samples. Data are displayed as mean  $\pm$  SEM. Statistical significance was determined using t-tests. (c) *Il23r*<sup>fl/fl</sup> and *Foxp3*<sup>Cre-YFP</sup>*Il23r*<sup>fl/fl</sup> mice were inoculated i.d. with B16 tumor cells, inoculated s.c. with YUMMER1.7 tumor

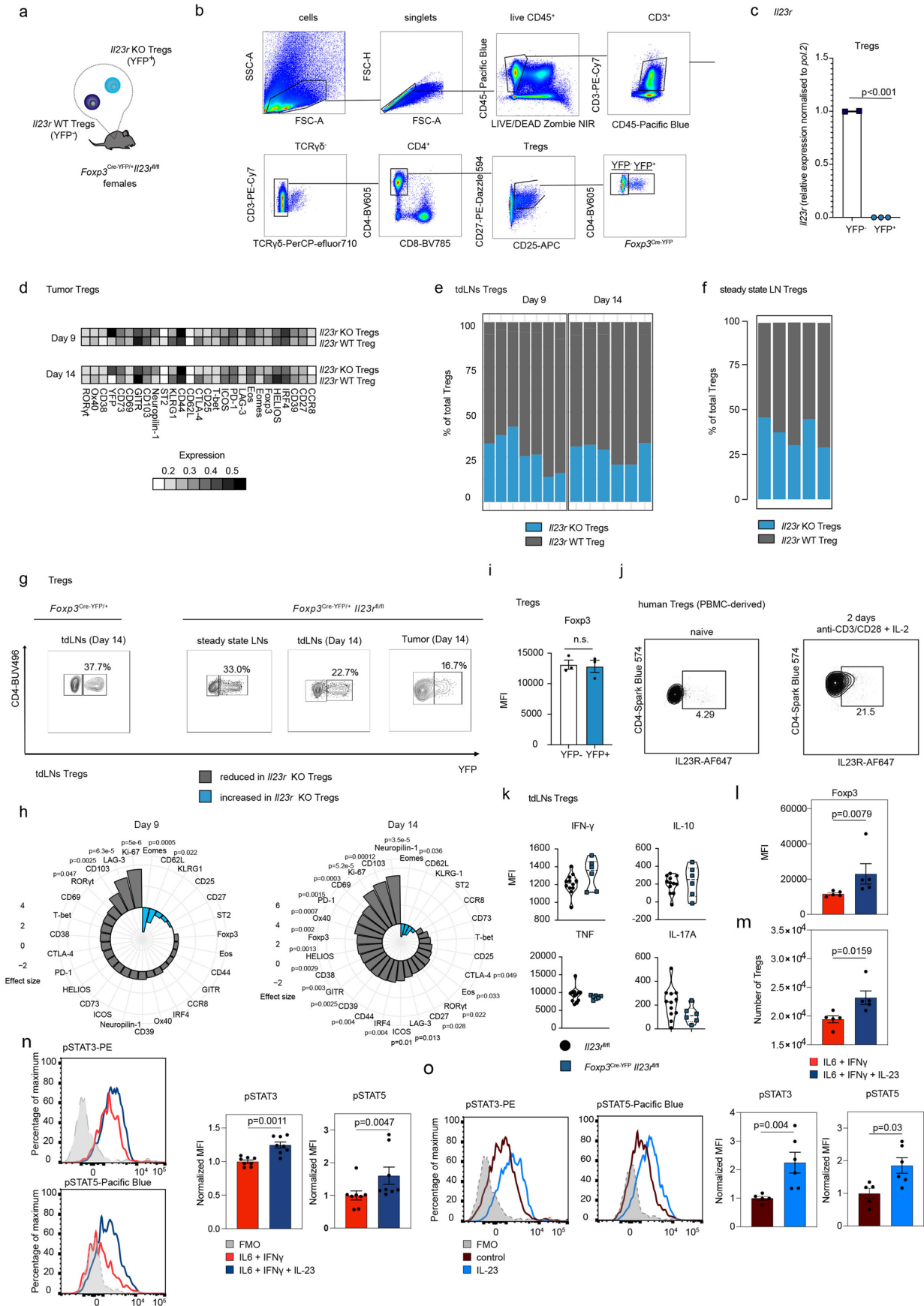
cells or inoculated s.c. with MC38 tumor cells. Tumors were analyzed on day 15, 14 or 24 post-inoculation. Pictures depict tumors after harvest. Data from 3 independent experiments with  $n = 6-10$ . (d) Kinetics of tumor volume measured by caliper gauge in B16 tumor cell-inoculated i.d. *Foxp3*<sup>Cre-YFP</sup> and *Foxp3*<sup>Cre-YFP</sup>*Il23r*<sup>fl/fl</sup> mice. Mean  $\pm$  SEM is displayed. Statistical significance was determined using 2-way Anovas.  $n = 4$  biologically independent animals. (e) Kinetics of tumor volume measured by caliper gauge in MC38 tumor cell-inoculated s.c. C57Bl/6 mice i.p. injected either with anti-p19 blocking or isotype antibodies.  $n = 6$  (isotype) and  $n = 7$  (anti p19 antibody) biologically independent animals. Mean  $\pm$  SEM is displayed. Statistical significance was determined using 2-way Anovas.



Extended Data Fig. 3 | See next page for caption.

**Extended Data Fig. 3 | IL23R signaling in Treg cells suppresses anti-tumor immunity.** (a-f) Il23r<sup>fl/fl</sup> and Foxp3<sup>Cre-YFP</sup>Il23r<sup>fl/fl</sup> mice were inoculated s.c. with MC38 tumor cells (a-c) or inoculated s.c. with YUMMER1.7 tumor cells (d-f) and tumor-infiltrating T cells were analyzed by flow cytometry on day 24 (a-c) or 14 (d-f) post-inoculation. TILs from MC38 tumors were re-stimulated with PMA/Ionomycin prior flow cytometry analysis. Data display 2 independent experiments with n = 6-10. (a, d) UMAP with overlaid FlowSOM clustering (left) (gated on CD45<sup>+</sup> TCRβ<sup>+</sup> and TCRγδ<sup>+</sup> cells) and heatmap depicting relative marker expression among identified cell clusters (right). (b, e) Violin plots depicting cell numbers of identified T cell clusters per gram tumor. Data are displayed as mean ± SEM. Statistical significance was determined using two-tailed Mann-Whitney U-tests. (c, f) Dotplots displaying median marker expression in identified T cell clusters comparing Foxp3<sup>Cre-YFP</sup> Il23R<sup>fl/fl</sup> and Il23R<sup>fl/fl</sup> mice. Color represents log(median expression Foxp3<sup>Cre-YFP</sup> Il23R<sup>fl/fl</sup> / median expression Il23R<sup>fl/fl</sup>);

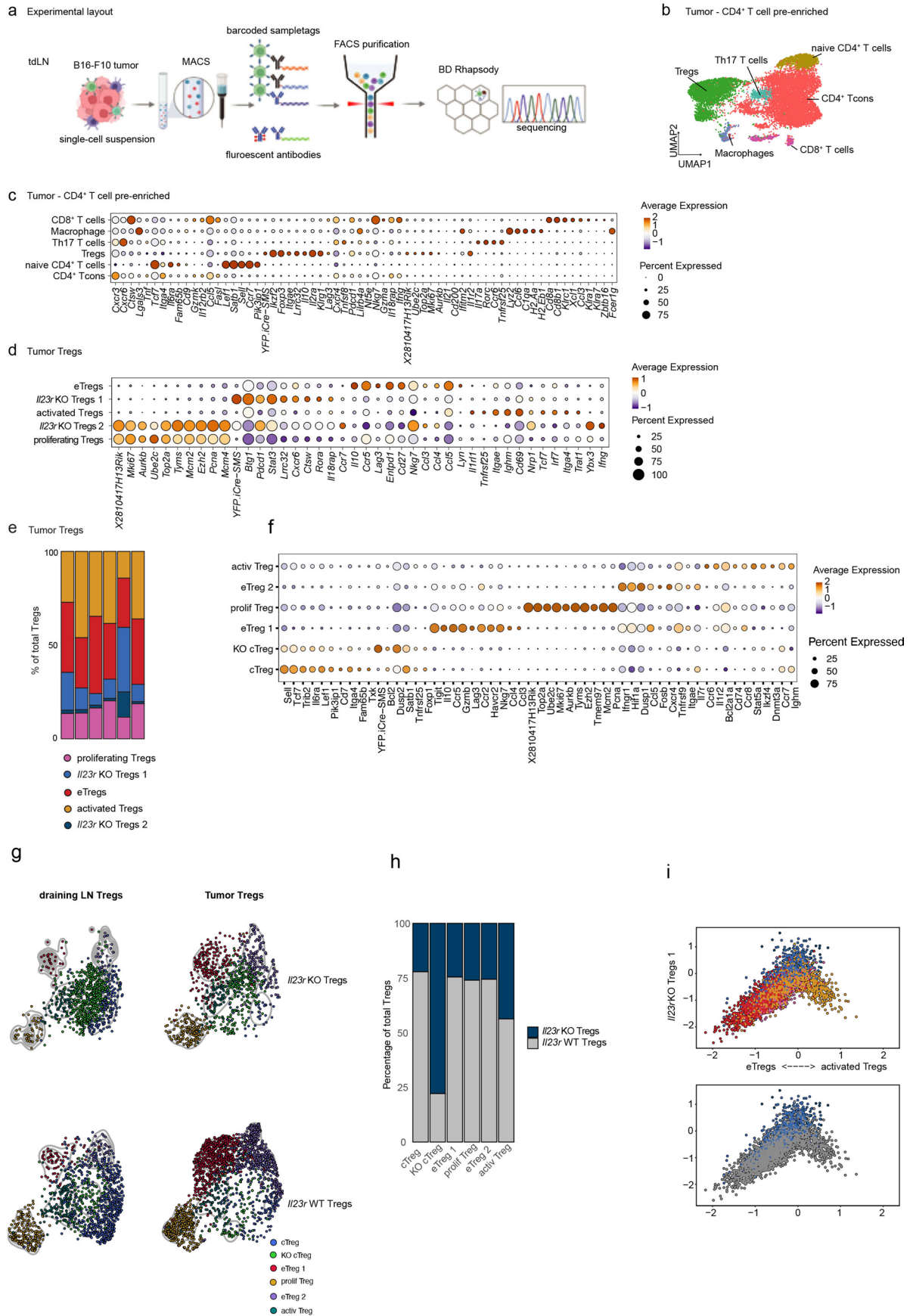
that is red means that median expression is decreased in Foxp3<sup>Cre-YFP</sup> Il23R<sup>fl/fl</sup> in comparison to Il23R<sup>fl/fl</sup> mice; green means that median expression is increased in Foxp3<sup>Cre-YFP</sup> Il23R<sup>fl/fl</sup> mice in comparison to Il23R<sup>fl/fl</sup> mice. Circle size represent log(p value). Statistically significant changes (p < 0.05) are highlighted with black lines around the circles. Statistical significance was determined using t-tests. (g) C57Bl/6 mice were s.c. inoculated with MC38 tumor cells and tumor-infiltrating T cells were analyzed by flow cytometry on day 14 post-inoculation. Dotplot displaying median marker expression of CD4<sup>+</sup> T cell and Treg cell clusters comparing anti-p19 and isotype antibody treated mice. Color represents log(median expression anti-p19/median expression isotype). Circle size represent log(p value). Statistically significant changes (p < 0.05) are highlighted with black lines around the circles. Data display one out of 2 independent experiments with n = 4-7. Statistical significance was determined using t-tests.



Extended Data Fig. 4 | See next page for caption.

**Extended Data Fig. 4 | IL23R signaling confers a selective advantage on eTreg cells.** (a) Schematic illustration of Tregs in  $\text{Foxp3}^{\text{Cre-YFP/+}} \text{Il23r}^{\text{fl/fl}}$  female mice. (b,c) FACS-gating strategy (b) and bar graphs (c) displaying  $\text{Il23r}$  mRNA expression levels as assessed by qPCR in  $\text{YFP}^+$  and  $\text{YFP}^-$  Treg cells from LNs of  $\text{Foxp3}^{\text{Cre-YFP/+}} \text{Il23r}^{\text{fl/fl}}$  female mice. Data depict one experiment with  $n = 2$  ( $\text{YFP}^+$ ) or  $n = 3$  ( $\text{YFP}^-$ ). (d-h)  $\text{Foxp3}^{\text{Cre-YFP/+}} \text{Il23r}^{\text{fl/fl}}$  female (d,e,f,h) and  $\text{Foxp3}^{\text{Cre-YFP/+}}$  non-floxed (g) mice were inoculated i.d. with B16 cells or left untreated. Treg cells in steady state LNs or tumor and tdLNs on day 9 or 14 post-inoculation were analyzed by flow cytometry. Data shown from one out of two independent experiments with  $n = 5-6$ . (d) Heatmap depicting marker expression among Treg cell clusters (tumor). (e, f) Frequency plots of  $\text{Il23r}$  KO and WT of total Treg cells in tdLNs (e) or steady state LNs (f). (g) Contour plots showing  $\text{YFP}^+$  Treg cells on day 14. (h) Spiral plot displaying differential marker expression between  $\text{Il23r}$  KO and WT Treg cells (tdLNs). (i) Bar graph displaying  $\text{Foxp3}$ -expression in  $\text{YFP}^+/\text{YFP}^-$  Treg cells (tdLNs) of  $\text{Foxp3}^{\text{Cre-YFP/+}}$  non-floxed mice on day 14 post-inoculation. Data from 1 experiment with  $n = 3$ . (j) Contour plots displaying  $\text{Il23R}$  expression as assessed by flow cytometry in human Tregs from steady state PBMCs (gated on  $\text{CD45}^+$

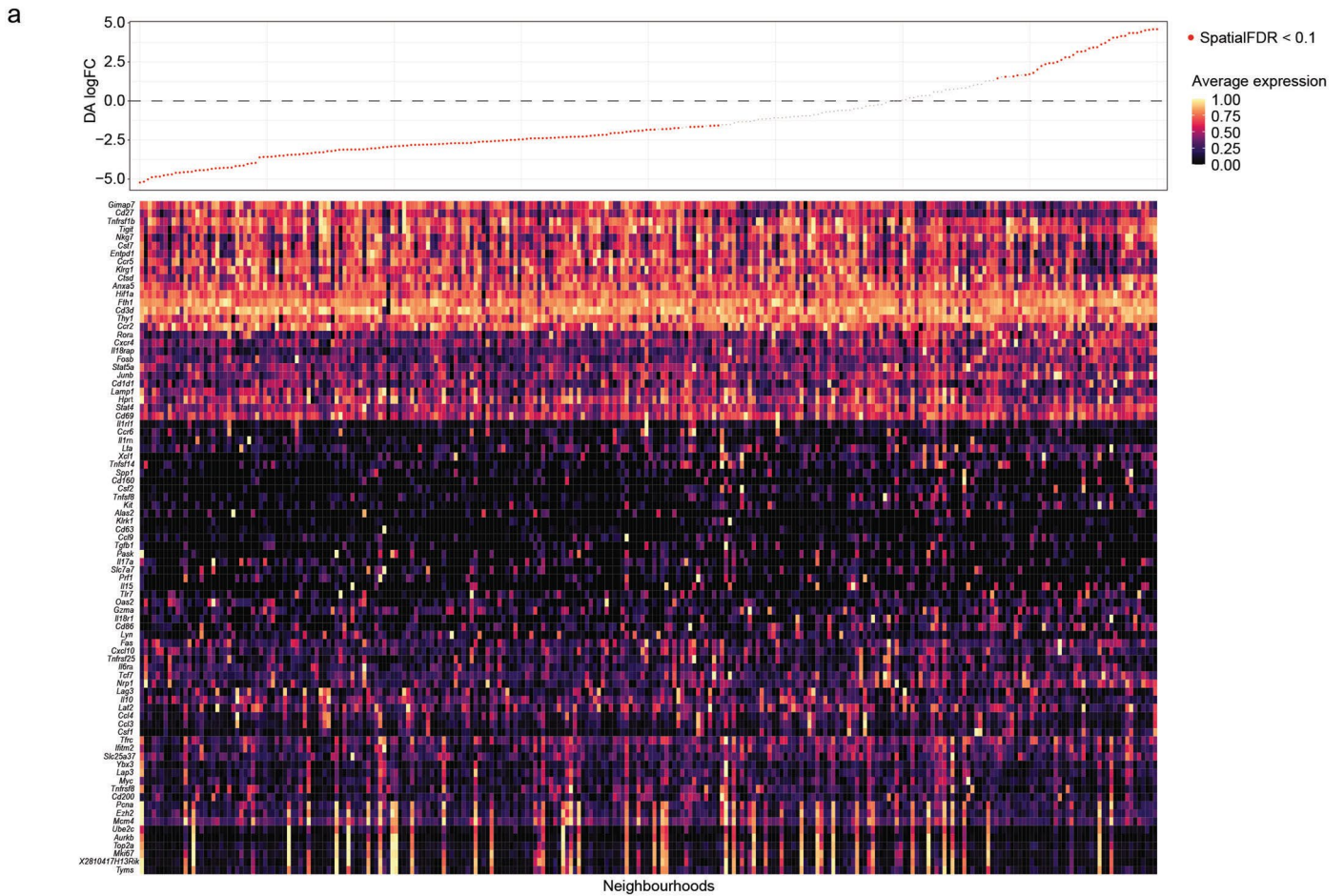
$\text{CD3}^+ \text{CD4}^+ \text{CD25}^+ \text{CD27}^+ \text{FOXP3}^+$  cells) or 2 days anti- $\text{CD3}/\text{CD28} + \text{IL-2}$  stimulated FACS sorted ( $\text{CD45}^+ \text{CD3}^+ \text{CD4}^+ \text{CD27}^+ \text{CD25}^+ \text{CD127}^-$  from steady state PBMCs) Tregs (gated on  $\text{CD45}^+ \text{CD3}^+ \text{CD4}^+ \text{CD25}^+ \text{CD27}^+ \text{FOXP3}^+$  cells). Data shown from one experiment with  $n = 2$ . (k)  $\text{Il23r}^{\text{fl/fl}}$  and  $\text{Foxp3}^{\text{Cre-YFP}} \text{Il23r}^{\text{fl/fl}}$  mice were inoculated i.d. with B16 cells. Treg cells in the tdLNs were analyzed by flow cytometry on day 14 post-inoculation. Violin plots displaying median expression (MFI) of cytokines. Data from one experiment with  $n = 6-12$ . (l,m,n) Murine Treg cells were ex vivo stimulated with  $\text{IFN-}\gamma + \text{IL-6}$ ,  $+/- \text{IL-23}$  for 5 days and analysed by flow cytometry. Boxplots showing the MFI of  $\text{Foxp3}$  (l) and total cell numbers (m). (l,m)  $n = 5$ . (n) Histograms (left) and boxplots showing normalized MFIs of  $\text{pSTAT3}/\text{pSTAT5}$  (right). Combined result from two independent experiments with  $n = 8$ . (o) Murine Treg cells were ex vivo stimulated with anti- $\text{CD3}/\text{CD28} + \text{IL-2}$  for 5 days and  $+/- \text{IL-23}$  for 30 min. Histograms (left) and boxplots showing normalized MFIs (flow cytometry). Representative result from two independent experiments with  $n = 5$  (control) or  $n = 6$  ( $\text{IL-23}$ ). (c,i,k,l,n,o) Data are displayed as mean  $\pm$  SEM. (c,h,i,k,l,n,o) Statistical significance was determined using, two-tailed t-test (c,h), t-tests (i,k,l) or the two-tailed Mann-Whitney U-test (n,o).



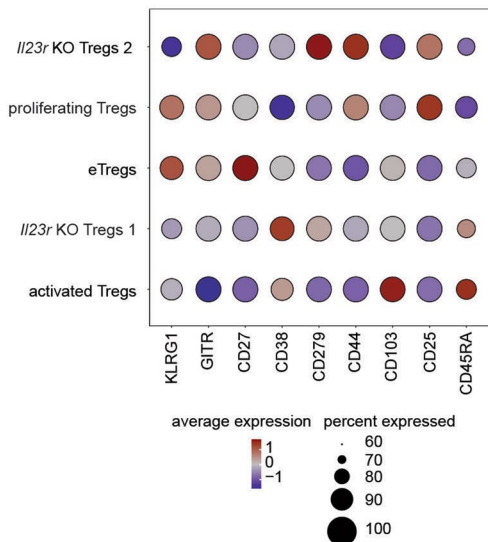
Extended Data Fig. 5 | See next page for caption.

**Extended Data Fig. 5 | IL-23 sensing by Treg cells initiates an eTreg cell program in the murine TME. (a-i)**  $Foxp3^{Cre-YFP/+}$  (heterozygous)  $Il23r^{fl/fl}$  female mice were inoculated i.d. with B16 tumor cells and combined transcriptome (scRNAseq) and protein expression analysis of sorted  $CD4^+$ T cells was performed on day 13 post-inoculation. Data shown from one experiment with  $n = 6$ . **(a)** Schematic illustration of the experimental workflow. **(b)** UMAP displaying clustered (based on transcriptome expression) and manually annotated cell subsets passing quality control. **(c)** Dotplot depicting the 10 most variable features in all identified cell subsets. **(d)** Dotplot displaying the 10 most

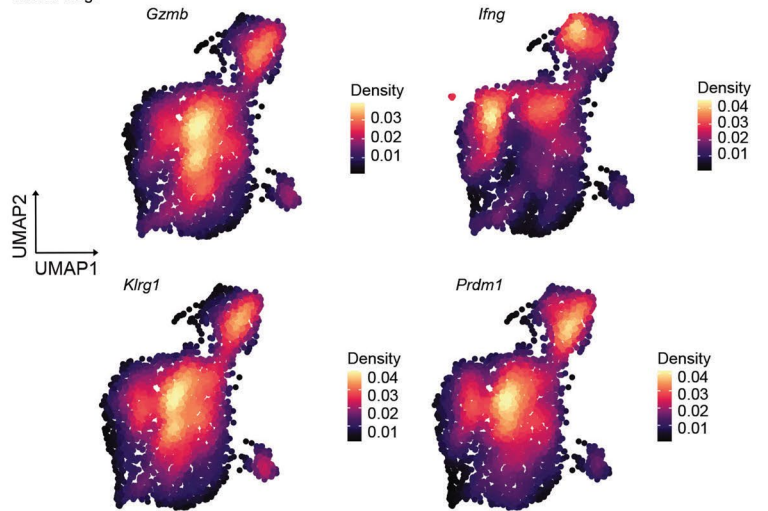
variable features across identified Treg cell subsets. **(e)** Bar chart displaying the frequencies of Treg cell subsets of total tumor Treg cells. **(f)** Dotplot of the most variable features of Treg cell subsets of integrated tumor and tumor-draining lymph node Treg cells. **(g)** UMAPs highlighting the distribution of  $Il23r$  KO and WT Treg cells across identified clusters in tumors and tumor-draining lymph nodes. **(h)** Bar chart of percentages of  $Il23r$  KO and WT Treg cells across Treg cell clusters. **(i)** Cellular state plot displaying enrichment of module scores of identified Treg cell subsets compared to gene modules of activated vs. eTreg cells (x-axis) and KO Treg cells (y-axis).



**c** Tumor Tregs - Protein



**b** Tumor Tregs



**Extended Data Fig. 6 | IL-23 sensing by Treg cells initiates an eTreg cell program in the murine TME. (a-c)** Foxp3<sup>Cre-YFP/+</sup> (heterozygous) Il23r<sup>fl/fl</sup> female mice were inoculated i.d. with B16 tumor cells and combined transcriptome (scRNAseq) and protein expression analysis of sorted CD4<sup>+</sup>T cells was performed on day 13 post-inoculation. **(a)** Log fold change of DA neighborhoods

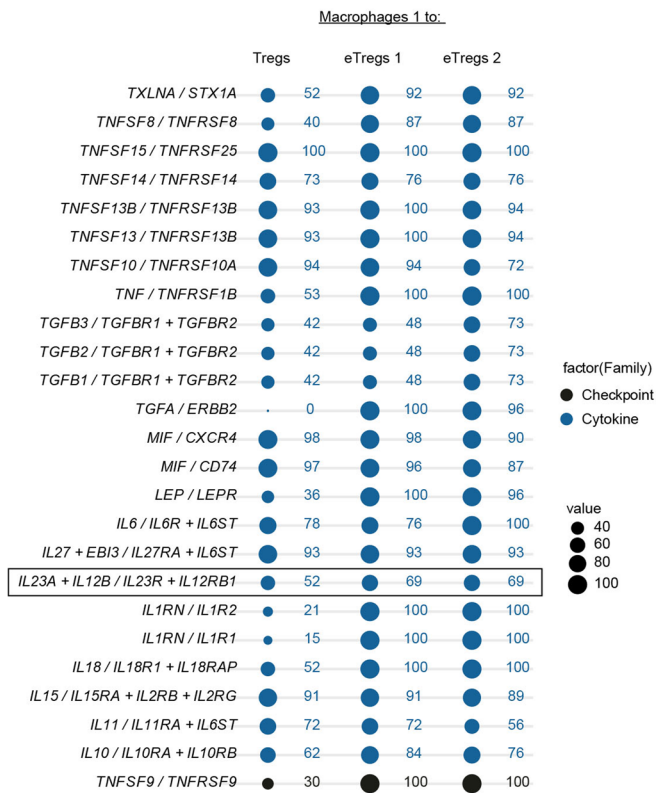
marked in red, neighborhoods with spatial FDR > 0.1 marked in grey (top). Heatmap depicting average gene expression of most variable markers across neighborhoods (bottom). **(b)** Dotplot depicting differentially expressed protein markers between the identified Treg cell clusters. **(c)** Expression density of selected variable features overlaid on UMAP displaying tumor Treg cells.



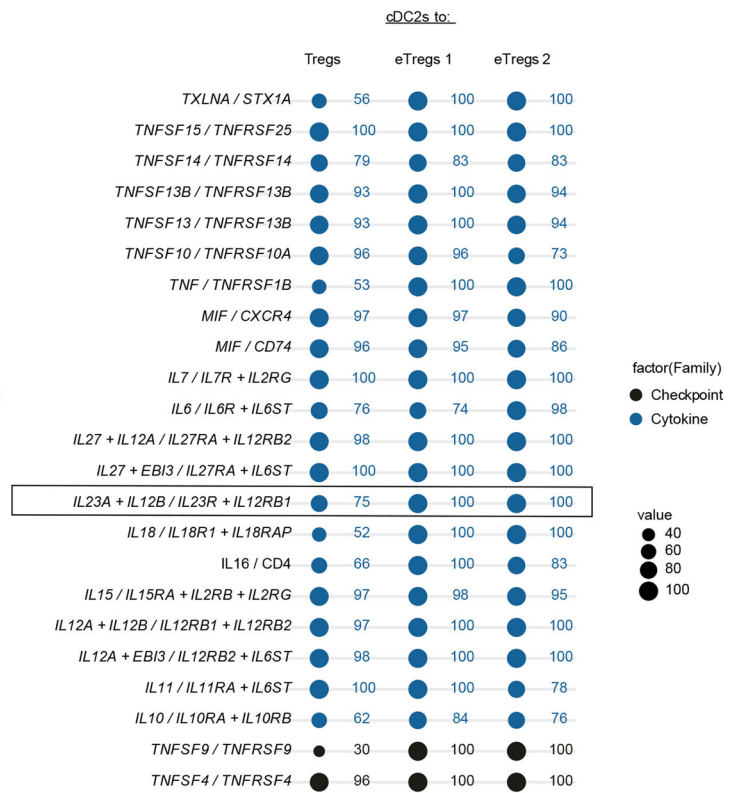
**Extended Data Fig. 7 | IL23R signaling induces an eTreg cell program in the human TME. (a–c)** Analyses of human myeloid pan-cancer single-cell sequencing data set from (Cheng et al. 2021) from  $n = 210$  individual patients across 15 human cancer types. **(a)** UMAP displaying pan-cancer myeloid cells. **(b)** UMAP depicting pan-cancer myeloid cells with overlaid IL23A expression. **(c)** Box plot displaying average IL23A expression in different pan-cancer myeloid cell clusters (grouped by cell type). Boxplots display the median and interquartile range (IQR; 25–75%) with whiskers representing the upper and lower quartile  $\pm$  IQR. **(d)** Box plot

displaying IL23R expression among Treg cells from patients with different cancer types. Boxplots display the median and interquartile range (IQR; 25–75%) with whiskers representing the upper and lower quartile  $\pm$  IQR. **(e–i)** Analyses of human pan-cancer single-cell sequencing data set from Zheng et al.<sup>41</sup> **(e, f, g, h)** and analyses of scRNAseq dataset of human colorectal carcinomas (Liu et al.<sup>43</sup>) **(i, j)**. **(g)** UMAP depicting pan-cancer CD8<sup>+</sup> T cells. **(e, h, i)** Heatmap depicting the expression of cell-type defining genes. **(f, j)** Dotplots showing the expression of selected cell lineage markers.

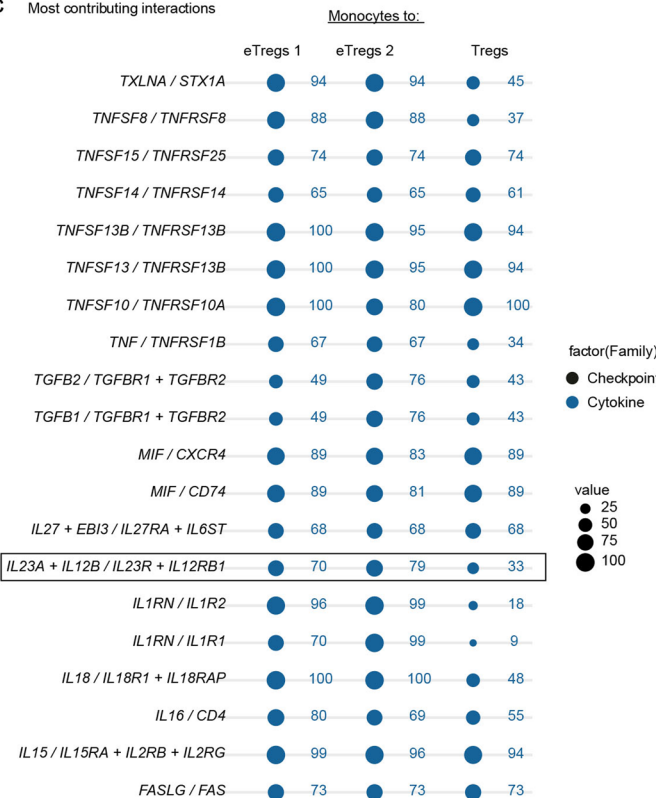
**a** Most contributing interactions



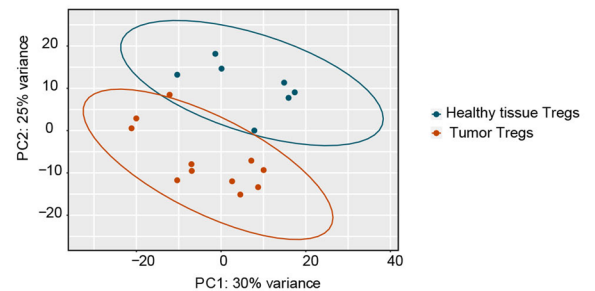
**b** Most contributing interactions



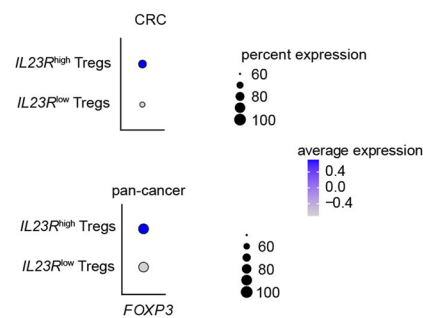
**c** Most contributing interactions



**d**



**e**



**Extended Data Fig. 8 | IL-23 signaling induces an eTreg cell program in the human TME.** (a–c) Analyses of scRNAseq dataset of human colorectal carcinomas (Liu et al.<sup>43</sup>). Dotplots displaying the top 25 statistically significant outgoing interactions from the macrophages 1 (a), cDC2s (b) or monocytes (c) cell clusters to Treg cell clusters computed with the ICELLNET framework. (d) PCA depicting data from bulk NGS data set from (Magnuson et al.<sup>27</sup>).

Comparison between Treg cells isolated from healthy colon biopsies and tumor tissue from colorectal cancer patients. (e) Dotplots displaying FOXP3 gene expression in IL23R<sup>high</sup> (IL23R expression > 0) and IL23R<sup>low</sup> (IL23R expression = 0) Treg cells from the human pan cancer T cell atlas (Zheng et al. 2021) and colorectal carcinoma (Liu et al.<sup>43</sup>) scRNA seq data sets.

## Reporting Summary

Nature Portfolio wishes to improve the reproducibility of the work that we publish. This form provides structure for consistency and transparency in reporting. For further information on Nature Portfolio policies, see our [Editorial Policies](#) and the [Editorial Policy Checklist](#).

### Statistics

For all statistical analyses, confirm that the following items are present in the figure legend, table legend, main text, or Methods section.

- |     |           |
|-----|-----------|
| n/a | Confirmed |
|-----|-----------|
- The exact sample size ( $n$ ) for each experimental group/condition, given as a discrete number and unit of measurement
  - A statement on whether measurements were taken from distinct samples or whether the same sample was measured repeatedly
  - The statistical test(s) used AND whether they are one- or two-sided  
*Only common tests should be described solely by name; describe more complex techniques in the Methods section.*
  - A description of all covariates tested
  - A description of any assumptions or corrections, such as tests of normality and adjustment for multiple comparisons
  - A full description of the statistical parameters including central tendency (e.g. means) or other basic estimates (e.g. regression coefficient) AND variation (e.g. standard deviation) or associated estimates of uncertainty (e.g. confidence intervals)
  - For null hypothesis testing, the test statistic (e.g.  $F$ ,  $t$ ,  $r$ ) with confidence intervals, effect sizes, degrees of freedom and  $P$  value noted  
*Give  $P$  values as exact values whenever suitable.*
  - For Bayesian analysis, information on the choice of priors and Markov chain Monte Carlo settings
  - For hierarchical and complex designs, identification of the appropriate level for tests and full reporting of outcomes
  - Estimates of effect sizes (e.g. Cohen's  $d$ , Pearson's  $r$ ), indicating how they were calculated

*Our web collection on [statistics for biologists](#) contains articles on many of the points above.*

### Software and code

Policy information about [availability of computer code](#)

**Data collection**

Flow cytometry data: Cytex Aurora 5L; SpectroFlo Software (v3.0 & v3.1).  
BD FACSAria™ 3L or 5L , FACS Diva Software v9.1.  
Immunofluorescence: Leica SP5 confocal microscope.  
BD Rhapsody single cell RNA sequencing: mouse cells were sorted using BD FACSAria™ 5L and loaded on the BD Rhapsody cartridges. Libraries were prepared according to the manufacturer's instructions and sequenced on an Illumina Novaseq S1.

**Data analysis**

Flow cytometry data:  
FlowJo software (v10, BD)  
Prism software (GraphPad v9)  
R-studio (v4.0 & v4.2.2). Mapping and clustering were performed using FlowSOM.

Single Cell RNA Sequencing:  
R (v4.0; v4.2.2), Seurat (v4.1.0 and v4.2.0) and scater (v. 1.26.1) for single cell RNA sequencing analyses. Milo (v1.7.0) for neighborhood analysis of mouse Tregs. SCpubr (v.1.0.4) for visualization of scRNAseq data. ICELLNET (v.1.00) for cell-cell communication analysis between myeloid cells and Tregs in human colorectal cancer. DESeq2 (v.1.37.4) for analysis of bulk RNA sequencing data. Monocle 3 was used for trajectory analysis.

For manuscripts utilizing custom algorithms or software that are central to the research but not yet described in published literature, software must be made available to editors and reviewers. We strongly encourage code deposition in a community repository (e.g. GitHub). See the Nature Portfolio [guidelines for submitting code & software](#) for further information.

## Data

Policy information about [availability of data](#)

All manuscripts must include a [data availability statement](#). This statement should provide the following information, where applicable:

- Accession codes, unique identifiers, or web links for publicly available datasets
- A description of any restrictions on data availability
- For clinical datasets or third party data, please ensure that the statement adheres to our [policy](#)

Single-cell sequencing data generated for this study have been deposited in the Gene Expression Omnibus (GEO) under accession number GSE224072. The accessibility of publicly available datasets used in this study is as follows : Human tumor-infiltrating T cell data from a pan cancer T cell atlas is available under the accession number GSE156728, scRNA-seq data from tumor-infiltrating leucocytes of colorectal cancer patients is accessible under the accession number GSE164522, bulk-RNA sequencing data of mouse and human tumor-infiltrating Tregs is accessible under the accession number GSE116347. Other data will be available from the corresponding authors upon request.

## Human research participants

Policy information about [studies involving human research participants and Sex and Gender in Research](#).

Reporting on sex and gender	NA
Population characteristics	NA
Recruitment	NA
Ethics oversight	NA

Note that full information on the approval of the study protocol must also be provided in the manuscript.

## Field-specific reporting

Please select the one below that is the best fit for your research. If you are not sure, read the appropriate sections before making your selection.

Life sciences       Behavioural & social sciences       Ecological, evolutionary & environmental sciences

For a reference copy of the document with all sections, see [nature.com/documents/nr-reporting-summary-flat.pdf](https://www.nature.com/documents/nr-reporting-summary-flat.pdf)

## Life sciences study design

All studies must disclose on these points even when the disclosure is negative.

Sample size	We did not perform sample size calculations. The sample size in flow cytometry experiments was greater than or equal to 3 mice per group. This is widely accepted in the field of immunology, if 2-3 independent experiments are performed. For single cell RNA sequencing processed on the BD Rhapsody platform 6 biological replicates were chosen, since only one independent experiment was performed. The chosen sample sizes are commonly used in the field of immunology and are similar to those in previous publications (Kim et al. Nature Immunology 2023, Wang et al. Nature Immunology 2020).
Data exclusions	No animals were excluded from the analysis. In the B16 experiment presented in figure 3 and MC38 experiment presented in Extended Data Figure 3 we excluded one outlier sample in each experiment, which we identified leveraging the ROUT method for detection of significant statistical outliers. For single cell RNA sequencing, Seven Bridges analysis was used to identify multiplets and cells that could not be linked to a sample tag. These cells were then excluded from further analysis.
Replication	Experiments were successfully repeated and the number of experiments is stated in the figure legends. Cytokine staining in MC38 model was performed once, as we used at least 7 mice per group and observed the same tumor phenotype as in the other tumor models. This also complies with the 3R principle in animal research.  scRNA sequencing was performed once, since sequencing results are highly robust due to the high number of individual cells, which are analyzed. In addition, scRNAseq experiments are cost-intensive and therefore it is common practice to only perform them once.
Randomization	Mice were grouped by genotype (when using Foxp3-Cre/Il23r floxed and Il23r floxed or Foxp3-Cre control mice), age and sex.
Blinding	Tumor inoculations and measurement of tumor size by caliper gauge were performed in a blinded fashion.

## Behavioural & social sciences study design

All studies must disclose on these points even when the disclosure is negative.

Study description	Briefly describe the study type including whether data are quantitative, qualitative, or mixed-methods (e.g. qualitative cross-sectional, quantitative experimental, mixed-methods case study).
Research sample	State the research sample (e.g. Harvard university undergraduates, villagers in rural India) and provide relevant demographic information (e.g. age, sex) and indicate whether the sample is representative. Provide a rationale for the study sample chosen. For studies involving existing datasets, please describe the dataset and source.
Sampling strategy	Describe the sampling procedure (e.g. random, snowball, stratified, convenience). Describe the statistical methods that were used to predetermine sample size OR if no sample-size calculation was performed, describe how sample sizes were chosen and provide a rationale for why these sample sizes are sufficient. For qualitative data, please indicate whether data saturation was considered, and what criteria were used to decide that no further sampling was needed.
Data collection	Provide details about the data collection procedure, including the instruments or devices used to record the data (e.g. pen and paper, computer, eye tracker, video or audio equipment) whether anyone was present besides the participant(s) and the researcher, and whether the researcher was blind to experimental condition and/or the study hypothesis during data collection.
Timing	Indicate the start and stop dates of data collection. If there is a gap between collection periods, state the dates for each sample cohort.
Data exclusions	If no data were excluded from the analyses, state so OR if data were excluded, provide the exact number of exclusions and the rationale behind them, indicating whether exclusion criteria were pre-established.
Non-participation	State how many participants dropped out/declined participation and the reason(s) given OR provide response rate OR state that no participants dropped out/declined participation.
Randomization	If participants were not allocated into experimental groups, state so OR describe how participants were allocated to groups, and if allocation was not random, describe how covariates were controlled.

## Ecological, evolutionary & environmental sciences study design

All studies must disclose on these points even when the disclosure is negative.

Study description	Briefly describe the study. For quantitative data include treatment factors and interactions, design structure (e.g. factorial, nested, hierarchical), nature and number of experimental units and replicates.
Research sample	Describe the research sample (e.g. a group of tagged <i>Passer domesticus</i> , all <i>Stenocereus thurberi</i> within Organ Pipe Cactus National Monument), and provide a rationale for the sample choice. When relevant, describe the organism taxa, source, sex, age range and any manipulations. State what population the sample is meant to represent when applicable. For studies involving existing datasets, describe the data and its source.
Sampling strategy	Note the sampling procedure. Describe the statistical methods that were used to predetermine sample size OR if no sample-size calculation was performed, describe how sample sizes were chosen and provide a rationale for why these sample sizes are sufficient.
Data collection	Describe the data collection procedure, including who recorded the data and how.
Timing and spatial scale	Indicate the start and stop dates of data collection, noting the frequency and periodicity of sampling and providing a rationale for these choices. If there is a gap between collection periods, state the dates for each sample cohort. Specify the spatial scale from which the data are taken
Data exclusions	If no data were excluded from the analyses, state so OR if data were excluded, describe the exclusions and the rationale behind them, indicating whether exclusion criteria were pre-established.
Reproducibility	Describe the measures taken to verify the reproducibility of experimental findings. For each experiment, note whether any attempts to repeat the experiment failed OR state that all attempts to repeat the experiment were successful.
Randomization	Describe how samples/organisms/participants were allocated into groups. If allocation was not random, describe how covariates were controlled. If this is not relevant to your study, explain why.
Blinding	Describe the extent of blinding used during data acquisition and analysis. If blinding was not possible, describe why OR explain why blinding was not relevant to your study.

Did the study involve field work?  Yes  No

# Reporting for specific materials, systems and methods

We require information from authors about some types of materials, experimental systems and methods used in many studies. Here, indicate whether each material, system or method listed is relevant to your study. If you are not sure if a list item applies to your research, read the appropriate section before selecting a response.

## Materials & experimental systems

n/a	Involved in the study
<input type="checkbox"/>	<input checked="" type="checkbox"/> Antibodies
<input type="checkbox"/>	<input checked="" type="checkbox"/> Eukaryotic cell lines
<input checked="" type="checkbox"/>	<input type="checkbox"/> Palaeontology and archaeology
<input type="checkbox"/>	<input checked="" type="checkbox"/> Animals and other organisms
<input checked="" type="checkbox"/>	<input type="checkbox"/> Clinical data
<input checked="" type="checkbox"/>	<input type="checkbox"/> Dual use research of concern

## Methods

n/a	Involved in the study
<input checked="" type="checkbox"/>	<input type="checkbox"/> ChIP-seq
<input type="checkbox"/>	<input checked="" type="checkbox"/> Flow cytometry
<input checked="" type="checkbox"/>	<input type="checkbox"/> MRI-based neuroimaging

## Antibodies

### Antibodies used

Anti-mouse antibodies including anti-CD279 (BV785, clone 29F.1A12, 1:200 dilution), anti-ICOS (BV750, clone C398.4A, 1:200 dilution), anti-NK1.1 (BV711, clone PK136, 1:150 dilution), anti-CD25 (BV650, clone PC61, 1:100 dilution), anti-CD152 (BV605, clone UC10-4B9, 1:200 dilution), anti-CD62L (BV570, clone MEL-14, 1:200 dilution), anti-Granzyme B (Pacific Blue, clone GB11, 1:50 dilution), anti-Neuropilin-1 (BV421, clone 3E+12, 1:200 dilution), anti-CD103 (Biotin, clone 2E7, 1:100 dilution), anti-Helios (PE-Cy7, clone 22F6, dilution 1:30), anti-TCR $\beta$  (PE-Cy5, clone H57-597, dilution 1:300), anti-KLRG1 (BV421, clone 2F1/KLRG1, dilution 1:200), anti-KLRG1 (PE-Dazzle 594, clone 2F1/KLRG1, dilution 1:400), anti-CD38 (APC-Fire 810, clone 90, dilution 1:400), anti-CCR8 (Spark NIR 685, clone SA214G2, dilution 1:200), anti-TIM-3 (APC, clone RMT3-23, dilution 1:400), anti-TIM-3 (PE-Fire 810, clone RMT3-23, dilution 1:400), anti-CD4 (Spark NIR 685, clone GK1.5, 1:250 dilution), anti-CD206 (Alexa Fluor 700, clone C068C2, dilution 1:600), anti-F4/80 (APC/Fire750, clone BM8, dilution 1:400), anti-CD86 (PE-Dazzle 594, clone GL1, 1:1200 dilution), anti-I-A/I-E (PE-Cy5, clone M5/114.15.2, 1:2000 dilution), anti-CD90.2 (Pacific Blue, clone 30-H12, 1:500 dilution), anti-CD11b (BV510, clone M1/70, 1:1500 dilution), anti-CD64 (BV605, clone X54-5/7.1, 1:100 dilution), anti-XCR1, clone ZET, 1:300 dilution), anti-Ly6C (BV711, clone HK1.4, 1:2000 dilution), anti-CX3CR1 (BV785, clone SA011F11, 1:400 dilution), anti-T-bet (BV711, clone 4B10, 1:50 dilution), anti-IRF4 (Pacific Blue, clone IRF4.3E4, 1:100 dilution), anti-GFP (Alexa Fluor 488, clone FM264G, 1:50 dilution), anti-CD45 (PE-Fire 810, clone S18009F, 1:150 dilution), anti-Ox40 (APC-Fire750, clone Ox-86, 1:200 dilution), anti-LAG-3 (custom conjugated to NovaFluor Blue 610/70S (dye purchased from ThermoFisher), clone C9B7W, 1:300 dilution), anti-TNF (BV711, clone MP6-XT22, 1:600 dilution), anti-IL-2 (BV510, clone JES6-5H4, 1:200), anti-IL-10 (PE-Dazzle 594, clone JES5-16E3, 1:200 dilution), were obtained from BioLegend. Anti-mouse antibodies including anti-CD69 (BUV395, clone H1.2F3, 1:100 dilution), anti-CD4 (BUV496, clone GK1.5, 1:400 dilution), anti-CD357 (BUV563, clone DTA-1, 1:400 dilution), anti-CD304 (BUV661, clone V46-1954, 1:400 dilution), anti-ST2 (BUV737, clone U29-93, 1:200 dilution), anti-CD8a (BUV805, clone 53-6.7, 1:150 dilution), anti-CD73 (BB660 custom conjugate, clone TY/23, 1:200 dilution), anti-Eomes (PE-CF594, clone X4-83, 1:100 dilution), anti-Eos (PE, clone W7-486, 1:200 dilution), anti-CD27 (R718, clone LG.3A10, 1:200 dilution), anti-Ki67 (BV480, clone B56, 1:200 dilution), anti-CD44 (BUV737, clone IM7, dilution 1:1200), anti-Ly6G (BUV563, clone 1A8, 1:700 dilution), anti-CD19 (BUV661, clone 1D3, 1:400 dilution), anti-CD45 (BUV395, clone 30-F11, 1:800 dilution), anti-CD172a (BUV395, clone P84, 1:100 dilution), anti-CD88 (BV750, clone 20/70, 1:200 dilution), anti-NK1.1 (BB700, clone PK136, 1:100 dilution), anti-Siglec-F (BB515, clone E50-2440, 1:2000 dilution) and IL-17A (PE, clone TC11-18H10, 1:600 dilution), BB630 Streptavidin (custom conjugate, 1:200 dilution) and BUV615 Streptavidin (custom conjugate, 1:200 dilution) were purchased from BD Biosciences. Anti-mouse antibodies including anti-Arginase-1 (APC, clone, dilution 1:400, A1ex5), anti-CD11c (PE-Cy5.5, clone N418, 1:1800 dilution), anti-NOS2 (PE-eFluor610, clone CXNFT, 1:800 dilution), anti-MerTK (PE-Cy7, clone DS5MMER, 1:200 dilution), anti-CD39 (PerCP-eFluor 710, clone 24DMS1, 1:400 dilution), anti-Foxp3 (PE-Cy5.5, clone FJK-16s, 1:200 dilution), anti-IFN $\gamma$  (PE-Cy7, clone XMG1.2, 1:400 dilution) and anti-IL-22 (APC, clone IL22JOP, 1:200 dilution) were purchased from ThermoFisher Scientific. Anti-TCF1 (Alexa Fluor 488, clone C63D9, 1:200 dilution) was obtained from Cell Signaling technologies. Anti-TOX (PE, clone REA473, 1:200 dilution) was purchased from Miltenyi. Anti human antibodies including anti-CD8 (BV785, clone RPA-T8, 1:100 dilution), anti-CD127 (BV605, clone A019D5, 1:50 dilution), anti-CD45 (Pacific Blue, clone HI-30, 1:200 dilution), anti-CD4 (Alexa Fluor 488, RPA-T4, 1:50 dilution), anti-CD25 (PE-Cy7, clone MA251, 1:40 dilution), anti-CD3 (APC, clone UCHT1, 1:100 dilution), anti-CD27 (BUV563, clone M-T271, 1:150 dilution) were either bought from BioLegend or BD. anti-IL23R (unconjugated, clone EPR22838-4, 1:100 dilution) was obtained from Abcam, secondary Goat anti-rabbit antibody (Alexa Fluor 647, 1:1000 dilution) was purchased from ThermoFisher.

### Validation

All antibodies used in our study are commercially available and have been titrated in-house. All antibodies have been validated by the commercial manufacturers. Validation data are available on the manufacturer's website.

## Eukaryotic cell lines

Policy information about [cell lines and Sex and Gender in Research](#)

### Cell line source(s)

B16-F10 cell line was originally received from Xenogen. MC38 cell line was received from Michael Dettmer and originally derived from American Type Culture Collection (ATCC). YUMMER1.7 cell line was purchased from Merck-Millipore.

### Authentication

None of the cell lines were authenticated in these studies, for experiments cell lines with low passage numbers were used.

Mycoplasma contamination	All cell lines used in the study tested negative for mycoplasma contamination.
Commonly misidentified lines (See <a href="#">ICLAC</a> register)	No commonly misidentified cell lines were used.

## Animals and other research organisms

Policy information about [studies involving animals](#); [ARRIVE guidelines](#) recommended for reporting animal research, and [Sex and Gender in Research](#)

Laboratory animals	B6.129(Cg)-Foxp3tm3(DTR/GFP)Ayr/J (Foxp3DTR-GFP) mice and B6.129(Cg)-Foxp3tm4(YFP/cre)Ayr/J (Foxp3Cre-YFP) mice were purchased from the Jackson Laboratory (J#016959). IL23rf1/fl mice were obtained from Philip Rosenstiel (Aden et al., 2016). IL23rf1/fl mice were crossed to a Deleter Cre mouse line CMV (Deleter) Cre (J#006054) to obtain IL23rdel/del mice. IL23RtdTomato mice were generated by Mohammed Oukka and Biocytogen plasmid construction service. All mice were maintained on a C57/BL6 background and were housed in a specific-pathogen-free environment. Both female and male mice were used for experiments at the age of 6-10 weeks. Mice were socially housed with a dark/light cycle of 12h, ambient temperature of 22°C and 45-65% humidity.
Wild animals	No wild animals were used.
Reporting on sex	Findings do not only apply to one sex. Sex of the animals was considered as part of assigning experimental groups. Sex-based analyses did not reveal differences.
Field-collected samples	No field-collected samples were used in the study.
Ethics oversight	All experiments were approved by the cantonal veterinary office of Zurich.

Note that full information on the approval of the study protocol must also be provided in the manuscript.

## Flow Cytometry

### Plots

Confirm that:

- The axis labels state the marker and fluorochrome used (e.g. CD4-FITC).
- The axis scales are clearly visible. Include numbers along axes only for bottom left plot of group (a 'group' is an analysis of identical markers).
- All plots are contour plots with outliers or pseudocolor plots.
- A numerical value for number of cells or percentage (with statistics) is provided.

### Methodology

Sample preparation	Tumors were minced into small pieces and digested in RPMI 2% FCS supplemented with 1mg/ml Collagenase IV and 100 µg/ml DNase I (both Sigma-Aldrich) at 37°C for 45 mins. After this, the tissue was disrupted with a syringe with an 18 G needle and digested for another 15mins. After digestion, the disrupted tissue was filtered through a 100 µm cell strainer and washed with PBS. LNs and thymi were grinded through 100 µm cell strainers and washed with PBS. Immune cell enrichment was performed using mouse CD45 TIL microbeads (Miltenyi Biotec) following the manufacturer's instructions. Ear skin was digested as previously described. In brief, skin was minced into small pieces and digested in RPMI 2% FCS supplemented with 1mg/ml Collagenase IV and 100 µg/ml DNase I (both Sigma-Aldrich) at 37°C for 1.5 hours. After digestion, the skin tissue was disrupted with a syringe with an 18-gauge needle and filtered through a 70-µm cell strainer. To isolate immune cells from murine colons, 6cm long pieces from the mid-colon were collected and washed with cold PBS. Isolated tissues were incubated in HBSS (without calcium/magnesium) supplemented with 2% FCS, 10mM HEPES and 5mM DTT at 80 rpm at 37°C for 8 mins, before being incubated 3 times in HBSS (without calcium/magnesium) supplemented with 2% FCS, 10mM HEPES, 5mM EDTA at 80 rpm at 37°C for 7 mins. Next, the colons were rinsed in HBSS (with calcium/magnesium) supplemented with 2% FCS and 10mM HEPES at 80 rpm at 37 °C for 5 mins. Then, the tissues were minced using a gentleMACS™ (Miltenyi Biotec) in digestion buffer (HBSS (with calcium/magnesium) supplemented with 3% FCS, 10mM HEPES, 30ug/ml DNase I and 100ug/ml Liberase TM) and incubated at 120 rpm at 37 °C for 25 mins before being filtered through 100-µm cell strainer and washed with cold PBS.
Instrument	Cells were analyzed using a Cytek Aurora 5L spectral flow cytometer, cells were sorted using a BD FACS Aria III 3L or 5L system.
Software	SpectroFlo (Cytek) or BD FACS Diva software was used for data acquisition, Flowjo (BD) v10 was used for data analysis.
Cell population abundance	For single cell RNA sequencing LIVE CD4+ T cells after FACS purification had a purity of >99% (based on FACS assessment). Human LIVE CD4+CD25+CD27+CD127- Tregs had a purity of >99% after FACS purification.
Gating strategy	FSC-A and SSC-A gating was applied to exclude debris, doublets were excluded by FSC-Area vs. FSC-Height gating. Dead cells

## Gating strategy

were excluded using Zombie NIR Live/Dead fixable staining reagent (BioLegend) or LIVE/DEAD Blue fixable staining reagent (ThermoFisher).

Gating strategies to identify cell populations of interest include:

$\gamma\delta$  T cells: CD45+CD3+TCR $\gamma\delta$ +

CD8+ T cells: CD45+CD3+CD8+CD4-

CD4+ Tcons: CD45+CD3+CD8-CD4+Foxp3-DTR-GFP-

Treg: CD45+CD3+CD8-CD4+Foxp3-DTR-GFP+ or CD45+CD3+CD8-CD4+Foxp3-Cre-YFP+

Il23r KO Treg: CD45+CD3+CD4+CD8-CD25+CD27+YFP+

Il23r WT Treg: CD45+CD3+CD4+CD8-CD25+CD27+YFP-

Human Treg: CD45+CD3+CD4+CD8-CD25+CD27+CD127-

Tick this box to confirm that a figure exemplifying the gating strategy is provided in the Supplementary Information.